Journal of the Mechanics and Physics of Solids 57 (2009) 1017–1044

Contents lists available at ScienceDirect

Journal of the Mechanics and Physics of Solids

journal homepage: www.elsevier.com/locate/jmps

Homogenization-based continuum plasticity-damage model for ductile failure of materials containing heterogeneities

Somnath Ghosh *, Jie Bai, Daniel Paquet

Department of Mechanical Engineering, The Ohio State University, 201 West 19th Avenue, Columbus, OH 43210, USA

ARTICLE INFO

Article history:
Received 25 May 2008
Received in revised form
31 March 2009
Accepted 2 April 2009

Keywords:
Homogenization
Anisotropic continuum plasticity-damage model
Ductile fracture
LE-VCFEM
Gurson–Tvergaard–Needleman model

ABSTRACT

This paper develops an accurate and computationally efficient homogenization-based continuum plasticity-damage (HCPD) model for macroscopic analysis of ductile failure in porous ductile materials containing brittle inclusions. Example of these materials are cast alloys such as aluminum and metal matrix composites. The overall framework of the HCPD model follows the structure of the anisotropic Gurson–Tvergaard–Needleman (GTN) type elasto-plasticity model for porous ductile materials. The HCPD model is assumed to be orthotropic in an evolving material principal coordinate system throughout the deformation history. The GTN model parameters are calibrated from homogenization of evolving variables in representative volume elements (RVE) of the microstructure containing inclusions and voids. Micromechanical analyses for this purpose are conducted by the locally enriched Voronoi cell finite element model (LE-VCFEM) [Hu, C., Ghosh, S., 2008. Locally enhanced Voronoi cell finite element model (LE-VCFEM) for simulating evolving fracture in ductile microstructures containing inclusions. Int. J. Numer. Methods Eng. 76(12), 1955–1992]. The model also introduces a novel void nucleation criterion from micromechanical damage evolution due to combined inclusion and matrix cracking. The paper discusses methods for estimating RVE length scales in microstructures with non-uniform dispersions, as well as macroscopic characteristic length scales for non-local constitutive models. Comparison of results from the anisotropic HCPD model with homogenized micromechanics shows excellent agreement. The HCPD model has a huge efficiency advantage over micromechanics models. Hence, it is a very effective tool in predicting macroscopic damage in structures with direct reference to microstructural composition.

1. Introduction

Metals and alloys containing heterogeneities e.g. particulates, intermetallics, or voids in their microstructure are widely used in automobile, aerospace and other engineering systems. Fig. 1(a) shows a micrograph of a cast aluminum alloy *A*319 containing eutectic silicon particles and a very small amount of brittle, copper-based intermetallics in an aluminum matrix. These heterogeneities can have adverse effects on failure properties like ductility and fracture toughness. Microstructural mechanisms in ductile failure include particulate fragmentation, interfacial debonding and matrix failure (Li et al., 1999; Moorthy and Ghosh, 1998). Failure initiates by particle cracking or interfacial debonding, after which voids grow near crack tips and subsequently coalesce to cause matrix failure. Crack initiation and propagation mechanisms are sensitive to local

* Corresponding author. Tel.: +1 614 292 2599; fax: +1 614 292 7369.
E-mail address: ghosh.5@osu.edu (S. Ghosh).

0022-5096/$ - see front matter © 2009 Elsevier Ltd. All rights reserved.
doi:10.1016/j.jmps.2009.04.002

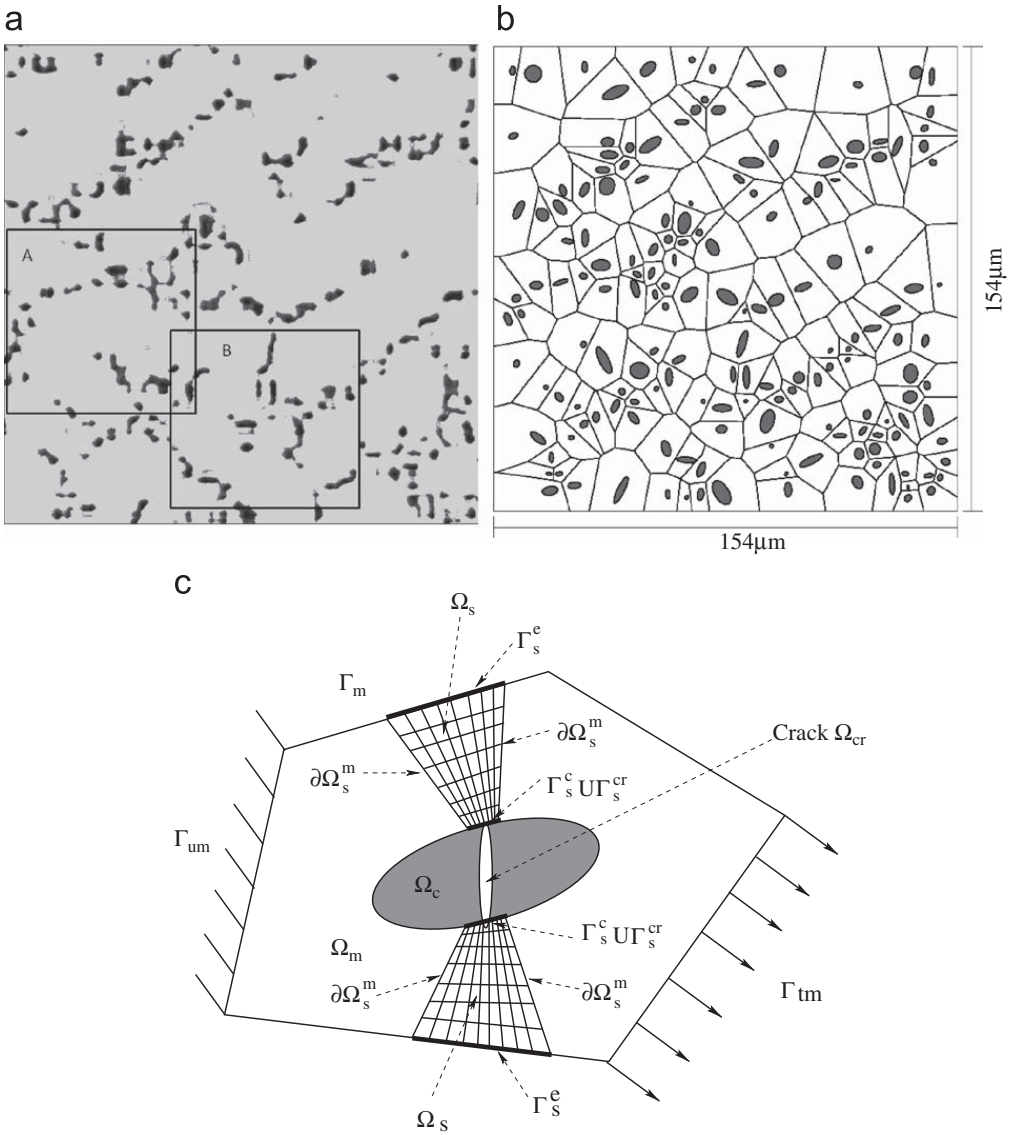

Fig. 1. (a) A micrograph of a cast aluminum alloy showing distribution of Si particles and intermetallics; (b) simulated microstructure, discretized into Voronoi cells by tessellation; (c) a typical Voronoi cell element with a cracked particle.

variations in morphological and constitutive parameters, as seen in the experimental studies in Wang (2003), Argon et al. (1975), and Caceres (1999). Modeling failure properties like ductility requires incorporation of microstructural morphology for accurate predictions.

It is prohibitive to conduct computational modeling of entire structures at the scale of the microstructure with explicit representation of heterogeneities. Various macroscopic constitutive models, based on phenomenological and micro-mechanical approaches, have been proposed to model heterogeneous material behavior and failure. Motivated by experimental observations, phenomenological theories introduce internal scalar or tensor damage variables, whose growth is governed by evolution laws. Most of these models do not explicitly account for microstructural variabilities or their interaction. Lack of microstructural morphology and information on underlying physics plague the application of these models for general use. In contrast, micromechanical models solve boundary value problems of the representative volume element (RVE) with microstructural details to predict constitutive response at the macroscopic level. Among various analytical micromechanical models are those based on effective medium approximations (Hashin, 1962; Mori and Tanaka, 1973) and those based on variational bounding methods e.g. Willis (1981) and Ponte Castaneda and Suquet (1998). These methods have limited capabilities for complex morphologies with high contrast in phase properties, material nonlinearities and non-proportional load histories.

Alternatively, multi-scale computational homogenization theories using asymptotic expansion (Benssousan et al., 1978; Sanchez-Palencia, 1980) have been used as popular tools for estimating averaged material properties of heterogeneous materials. Concurrent finite element analyses are executed at macro- and microscales with information transfer between them. Competent methods have evolved using this approach in Guedes and Kikuchi (1990), Fish et al. (1999), Terada and Kikuchi (2001), Kouznetsova et al. (2001), and Feyel and Chaboche (2000). Moulinec and Suquet (1998) have developed a

fast Fourier transform-based computational model for evaluating the effective response of linear and nonlinear periodic composite materials. However, this method is incapable of modeling materials with high contrast in phase properties, e.g. materials with voids and rigid inclusions. To overcome this limitation, the authors have subsequently enhanced this method with an augmented Lagrangian-based methodology for composites with infinite phase contrast in Moulinec and Suquet (2001). The paper develops elastic plastic models for materials with voids and power law creep models for rigid inclusion composites.

Ghosh and co-workers have combined the asymptotic homogenization method with the micromechanical Voronoi cell finite element method (VCFEM) for multi-scale analysis of deformation and damage in non-uniformly distributed microstructures in Ghosh et al. (1995, 1996, 2001) and Ghosh (2008). However, such approaches can be computationally very expensive since detailed micromechanical analyses should be conducted for every integration point of macroscopic elements. Terada and Kikuchi (1995) have replaced micromechanical analysis by an extensive numerical database in the strain space, which is not reliable for path and history dependent problems. To overcome the shortcomings of simultaneous macro–micro modeling in predicting deformation with damage, Raghavan and Ghosh (2005) and Jain and Ghosh (2008a, b) have developed computationally efficient, anisotropic homogenization-based continuum damage mechanics (HCDM) models for brittle composites undergoing fiber-matrix interface debonding. The reduced order models are constructed from the results of homogenizing evolving damage variables in micromechanical analyses of a composite RVE. The HCDM models have been successfully deployed for macroscopic simulations in a multi-scale modeling framework for composites undergoing fiber-matrix interfacial debonding in Ghosh et al. (2007). The use of a continuum damage mechanics model in regions of non-localized damage evolution makes the overall computing in a multi-scale model, extremely efficient.

A *homogenization-based continuum plasticity-damage* or *HCPD* model is developed in this paper for ductile materials containing heterogeneities that are undergoing ductile failure with evolving porosity. The model follows a porous plasticity constitutive framework established in the Gurson–Tvergaard–Needleman or GTN models of Gurson (1977), Chu and Needleman (1980), Tvergaard (1982) and Tvergaard and Needleman (1984) that account for void nucleation, growth and coalescence. Shape parameters have been introduced in the GTN models (Devaux et al., 1997; Pardoen and Hutchinson, 2000; Benzerga et al., 2004; Siruguet and Leblond, 2004). Anisotropic GTN models with matrix anisotropy characterized by Hill's quadratic yield criterion have been proposed in Liao et al. (1997), Wang et al. (2004), Grange et al. (2000) and Benzerga et al. (2004). Studies on effective properties of porous material containing rigid particles in Garajeu and Suquet (1997) have shown that the yield surface retain the form of GTN model. A multi-scale micromorphic theory has been used in Vernerey et al. (2008) to develop a three-scale constitutive model to represent failure of high strength steel alloys due to nucleation, growth and coalescence of voids from each population of particles. They have not considered anisotropy due to the heterogeneities. A specific focus of the model proposed in this study is on the combination of tools in microstructure characterization and modeling to develop constitutive and damage models for heterogeneous microstructures as obtained from real micrographs. The model can be effectively used in simulations of ductile fracture with huge efficiency advantages over the micromechanics models, due to its significant reduced order. A few highlights of the proposed model are:

- The HCPD model evolves from rigorous homogenization of microscopic representative volume elements following the Hill–Mandel postulate. Micromechanical analyses of the RVEs with particle and matrix cracking are conducted with the locally enriched Voronoi cell finite element model or LE-VCFEM developed by Ghosh et al. (Moorthy and Ghosh, 1998; Hu et al., 2007; Hu and Ghosh, 2008).
- The HCPD model modifies the GTN model to account for the presence of non-uniform dispersion of inclusions in the microstructural RVE. This gives rise to strong anisotropy in the constitutive relations. With increasing deformation in the microstructure, the anisotropy will evolve due to constrained plastic flow. The HCPD model introduces a unique anisotropic plastic flow potential, in which parameters evolve as functions of the deformation variables and plastic work. Effects of load history and path dependence on deformation and evolving damage variables are accounted for in the model through projection on an evolving principal material coordinate system. Functional forms of material parameters in the HCPD model are constructed by homogenizing plasticity and damage variables from micromechanical analyses of the representative volume element. Very little literature exists that considers this anisotropy and its evolution in the plasticity-damage model. Furthermore, the model includes a non-local void growth law to avoid mesh sensitivity, especially during softening.
- A novel macroscopic crack nucleation criterion, induced by particle cracking in the microstructure, is also developed from homogenizing data on inclusion fragmentation in the RVE. The model is directly based on the observed Weibull distribution functions governing particle cracking in the microstructure.
- The HCPD model uses statistical methods of microstructure characterization to estimate the RVE size and non-local characteristic length scale in real material microstructures. This is an important feature in comprehensive models for ductile failure in heterogeneous materials.

Section 2 in this paper introduces computational tools for developing the homogenization-based continuum plasticity-damage model. Major elements of the non-local anisotropic HCPD model are developed in Section 3. Various numerical examples, validating the model are discussed in Section 4.

2. Computational tools for developing the HCPD model

This section introduces several essential computational tools that are necessary for developing the anisotropic homogenization-based continuum plasticity-damage model for porous ductile materials containing non-uniform dispersion of brittle inclusions. Description of these tools are brief and references are provided for detailed understanding of these methods.

2.1. Micromechanical analyses: locally enriched Voronoi cell finite element model

The Voronoi cell finite element model has been developed by Ghosh and coworkers (Moorthy and Ghosh, 1998, 2000; Ghosh and Moorthy, 1998) for modeling microstructures with non-uniform dispersion of heterogeneities. VCFEM offers significant advantages in efficient and accurate micromechanical analysis. Morphological arbitrariness in dispersions, shapes and sizes of heterogeneities, as seen in real micrographs are readily modeled by this method. Earlier developments in modeling microstructural damage inception by particulate cracking in Moorthy and Ghosh (1998) and Ghosh and Moorthy (1998) has recently been extended to model ductile failure by a locally enriched VCFEM or LE-VCFEM in Hu et al. (2007) and Hu and Ghosh (2008). In LE-VCFEM, ductile fracture initiates with inclusion cracking in the microstructure and evolves with matrix cracking in the form of void nucleation, growth and coalescence. Details of the LE-VCFEM formulation are provided in Hu and Ghosh (2008). Fig. 1(a) shows a multi-phase material microstructural section, which is discretized into a network of Voronoi cells as shown in Fig. 1(b). As shown in Fig. 1(c), the matrix and inclusion phases in each Voronoi cell are designated as Ω_m and Ω_c, respectively, while the inclusion crack phase is labeled as Ω_{cr}. Each Voronoi cell, containing the inclusion and crack phases in the matrix, is designated as an element in the Voronoi cell finite element (VCFE) formulation. In ductile fracture, inclusion cracking is often followed by localized ligaments of intense void evolution. This results in a transition of the local stress–strain response from hardening to the softening behavior. The assumed stress-based VCFEM is *adaptively* augmented with a patch of high-resolution displacement-based finite elements in regions of strain softening Ω_s within each Voronoi cell element, as shown in Fig. 1(c). Finite deformation elasto-porous plasticity formulation governs the behavior of displacement-based elements in Ω_s.

The matrix phase in each Voronoi cell element is modeled using a rate independent non-local GTN model (Chu and Needleman, 1980; Tvergaard and Needleman, 1984, 1995), for which the evolving yield surface is written as

$$\Phi = \left(\frac{q}{\sigma_0}\right)^2 + 2f^* q_1 \cosh\left(-\frac{3q_2 p}{2\sigma_0}\right) - (1 + q_3 f^{*2}) = 0 \tag{1}$$

where q is the Von-Mises stress, p is the hydrostatic pressure, σ_0 is equivalent tensile flow stress, f is void volume fraction, and q_1, q_2, q_3 are material constants. The evolution of void volume fraction is divided into growth and nucleation components:

$$\dot{f}^{local} = \dot{f}_{growth} + \dot{f}_{nucleation} \tag{2}$$

The superscript *local* corresponds to the contribution of only local variables to void evolution. Due to plastic incompressibility, the void growth rate in the matrix is written as

$$\dot{f}_{growth} = (1 - f)\dot{\varepsilon}^p_{kk} \tag{3}$$

Void nucleation is assumed to be plastic strain controlled as suggested in Chu and Needleman (1980) and its rate is expressed in terms of the effective plastic strain $\bar{\varepsilon_0}^p$ in matrix as

$$\dot{f}_{nucleation} = A(\bar{\varepsilon_0}^p)\dot{\bar{\varepsilon}}_0^{\,p} \tag{4}$$

where

$$A(\bar{\varepsilon_0}^p) = \frac{f_N}{s_N\sqrt{2\pi}} \exp\left[-\frac{1}{2}\left(\frac{\bar{\varepsilon_0}^p - \varepsilon_N}{s_N}\right)^2\right] \tag{5}$$

Here ε_N is the mean strain for nucleation, s_N is its standard deviation, and f_N is the volume fraction of void nucleating particles. The acceleration function f^* has been introduced by Tvergaard and Needleman (1984) to model the complete loss of material stress carrying capacity due to void coalescence as

$$f^* = \begin{cases} f, & f \leqslant f_c \\ f_c + \dfrac{f^*_u - f_c}{f_f - f_c}(f - f_c), & f > f_c \end{cases} \tag{6}$$

Here f_c is the critical void volume fraction at which void coalescence first occurs and f_f is the value at final failure.

To avoid mesh sensitivity of the FEM solution, f at a point $\bar{\mathbf{x}}$ is integrated from a non-local void evolution rate $\dot{f}$. This is evaluated from the local rate $\dot{f}^{local}$ using a non-local formula proposed in Tvergaard and Needleman (1995) as

$$\dot{f} = \frac{1}{W(\mathbf{x})}\int_{\Omega_m} \dot{f}^{local}(\mathbf{x}) w(|\mathbf{x}-\bar{\mathbf{x}}|)\,\mathrm{d}\Omega \tag{7}$$

where

$$W(\bar{\mathbf{x}}) = \int_{\Omega_m} w(|\mathbf{x}-\bar{\mathbf{x}}|)\,\mathrm{d}\Omega \quad \text{and} \quad w(|\mathbf{x}|) = \left[\frac{1}{1+(|\mathbf{x}|/L)^p}\right]^q \tag{8}$$

with $p=8,\ q=2$ and a material characteristic length $L>0$. The weighting function $w(|\mathbf{x}|)=1$ at $|\mathbf{x}|=0$, $w(|\mathbf{x}|)=0.25$ at $|\mathbf{x}|=L$ and $w(|\mathbf{x}|)\to 0\ \forall |\mathbf{x}|>L$ with a narrow transition region.

2.1.1. Criterion for inclusion cracking in the Voronoi cell elements

Inclusions in each Voronoi cell element are assumed to be isotropic, linear elastic. Instantaneous splitting of inclusions is assumed once a crack initiation criterion is satisfied at a point in the inclusion. A Weibull statistics-based criterion is invoked, where initiation occurs when the probability function P_{fr} (Li et al., 1999) exceeds a critical value (95% in the present work). The probability function is defined as

$$P_{fr}(v,\sigma_I^c) = 1 - \exp\left[-\frac{v}{v_0}\left(\frac{\sigma_I^c}{\sigma_w}\right)^m\right] \tag{9}$$

where m and σ_w are the Weibull modulus and the characteristic strength, respectively, v_0 is a reference volume, and σ_I^c is the maximum principal stress at a point in the inclusion. An elliptical crack is then introduced in the inclusion normal to the maximal principal stress direction. The Weibull parameters σ_w and m are calibrated from experiments using a procedure that is described in Hu and Ghosh (2008), yielding very good agreement with experiments.

2.2. Homogenization of micromechanical variables in RVE analysis

Development of the homogenized continuum plasticity-damage model requires evaluation of material properties from homogenized stresses, strains and other variables. The asymptotic expansion homogenization method has been developed in Benssousan et al. (1978), Sanchez-Palencia (1980), Guedes and Kikuchi (1990), Fish et al. (1999) and Terada and Kikuchi (2001) for homogenized constitutive models of heterogeneous materials. Ghosh et al. have introduced a novel implementation of the asymptotic homogenization method, coupling macroscopic analysis with micromechanical VCFEM analysis of the RVE, in Ghosh et al. (1996, 2001, 2007) and Raghavan and Ghosh (2005). In the present work, the asymptotic homogenization method is implemented in conjunction with micromechanical elastic–plastic damage analysis of the RVE Y by LE-VCFEM. A small variant of the Voronoi cell element formulation in Hu and Ghosh (2008) is needed for the energy functional in the RVE Y. Y-periodic displacement conditions are applied on ∂Y. This results in Y-anti-periodic tractions on ∂Y and hence there are no traction boundaries. A macroscopic strain $\bar{e}_{ij}$ is imposed on Y. The corresponding incremental energy functional for each Voronoi cell element is written as

$$\begin{aligned}\Pi_e^\varepsilon = &-\int_{Y_e\setminus Y_s}\frac{1}{2}(S^{\tan}_{ijkl})^\varepsilon \Delta\sigma^\varepsilon_{ij}\Delta\sigma^\varepsilon_{kl}\,\mathrm{d}Y - \int_{Y_e\setminus Y_s} e^\varepsilon_{ij}\Delta\sigma^\varepsilon_{ij}\,\mathrm{d}Y + \int_{\partial Y_e}(\sigma^\varepsilon_{ij}+\Delta\sigma^\varepsilon_{ij})(u^\varepsilon_i+\Delta u^\varepsilon_i)n^e_j\,\mathrm{d}\partial Y\\ &-\int_{\partial Y_c}(\sigma^{\varepsilon m}_{ij}+\Delta\sigma^{\varepsilon m}_{ij}-\sigma^{\varepsilon c}_{ij}-\Delta\sigma^{\varepsilon c}_{ij})(u^{\varepsilon'}_i+\Delta u^{\varepsilon'}_i)n^c_j\,\mathrm{d}\partial Y - \int_{\partial Y_{cr}}(\sigma^{\varepsilon c}_{ij}+\Delta\sigma^{\varepsilon c}_{ij})(u^{\varepsilon''}_i+\Delta u^{\varepsilon''}_i)n^{cr}_j\,\mathrm{d}\partial Y - \int_{Y_s}\frac{1}{2}E^{\tan}_{ijkl}\Delta e^{\varepsilon s}_{ij}e^{\varepsilon s}_{kl}\,\mathrm{d}Y\\ &-\int_{Y_s}\sigma^{\varepsilon s}_{ij}\Delta e^{\varepsilon s}_{ij}dY + \int_{\partial Y_s}(\sigma_{ij}+\Delta\sigma_{ij})(u^s_i+\Delta u^s_i)n^s_j d\partial Y + \int_{Y_e\setminus Y_s}(\bar{e}_{ij}+\Delta\bar{e}_{ij})\Delta\sigma^\varepsilon_{ij}\,\mathrm{d}Y + \int_{Y_s}(\bar{e}_{ij}+\Delta\bar{e}_{ij})E^{\tan}_{ijkl}\Delta e^{\varepsilon s}_{kl}\,\mathrm{d}Y\end{aligned} \tag{10}$$

where $(S^{\tan}_{ijkl})^\varepsilon$ and $E^{\tan}_{ijkl}$ are the instantaneous elastic–plastic compliance and stiffness tensors, respectively. Here Y_e is the domain of each Voronoi cell element and Y_s is the region of displacement-based enrichment. Variables with superscript ε represent association with the microscale. Here ε is a small positive number corresponding to the ratio of microscopic and macroscopic scales. The equilibrated microscopic stress increment is represented by $\Delta\boldsymbol{\sigma}^\varepsilon$ in Eq. (10) and the microstructural strain increments are designated as $\Delta\boldsymbol{e}^\varepsilon$. The superscripts m, c, cr and s correspond to variables associated with the matrix, inclusion, crack and the enriched displacement-based region in each Voronoi cell element. Increments of microscopic displacements on each cell element boundary (∂Y_e), inclusion-matrix interface (∂Y_c) and crack boundary (∂Y_{cr}) are identified with $\Delta\boldsymbol{u}^\varepsilon$, $\Delta\boldsymbol{u}^{\varepsilon'}$, $\Delta\boldsymbol{u}^{\varepsilon''}$, respectively. The last two terms in Eq. (10) incorporates the effect of macroscopic strain $\bar{e}_{ij}$ in the microstructure. The stationarity condition of Π^ε_e with respect to stress increment $\Delta\sigma^\varepsilon_{ij}$ yields, as Euler's equations, the incremental form of the multi-scale *kinematic relations* in the matrix and inclusion regions of each element Y_m and Y_c, respectively, as

$$e^\varepsilon_{ij}+\Delta e^\varepsilon_{ij} = \bar{e}_{ij}+\Delta\bar{e}_{ij}+\frac{1}{2}\left[\frac{\partial(u_i+\Delta u_i)}{\partial y_j}+\frac{\partial(u_j+\Delta u_j)}{\partial y_i}\right] \quad \forall \mathbf{y}\in Y_m, Y_c \tag{11}$$

In addition, setting the first variation of Π_e^ε with respect to $\Delta\mathbf{u}^s$ in Y_s to zero, yields the constitutive relations in terms of stress perturbations as

$$\sigma_{ij}^s + \Delta\sigma_{ij}^s = \sigma_{ij} + \Delta\sigma_{ij} + E_{ijkl}^{\tan}(\bar{e}_{kl} + \Delta\bar{e}_{kl}) \quad \text{in } Y_s \tag{12}$$

Stationary conditions of the total energy functional $\Pi = \sum_{e=1}^{N} \Pi_e^\varepsilon$ in $\mathbf{Y}$ yield the inter-element, interface and crack boundary traction reciprocity conditions and other compatibility conditions as Euler's equations (Hu and Ghosh, 2008; Moorthy and Ghosh, 2000).

The incremental form of the homogenized stress–strain relation $\Delta\Sigma_{ij} = E_{ijkl}^H \Delta\bar{e}_{kl}$ is obtained by volume averaging stresses and strains over the RVE. For this, the LE-VCFEM generated microstructural variables are integrated as

$$\begin{aligned}
\Sigma_{ij} &= \frac{1}{Y}\int_Y \sigma_{ij}^\varepsilon(y)\,\mathrm{d}Y = \frac{1}{Y}\left[\int_{Y_m\setminus Y_s} \sigma_{ij}^\varepsilon\,\mathrm{d}Y + \int_{Y_c} \sigma_{ij}^\varepsilon\,\mathrm{d}Y + \int_{Y_s} \sigma_{ij}^\varepsilon\,\mathrm{d}Y\right] \\
\bar{e}_{ij} &= \frac{1}{Y}\int_Y e_{ij}^\varepsilon(y)\,\mathrm{d}Y = \frac{1}{Y}\left[\int_{Y_m\setminus Y_s} e_{ij}^\varepsilon\,\mathrm{d}Y + \int_{Y_c} e_{ij}^\varepsilon\,\mathrm{d}Y + \int_{Y_s} e_{ij}^{\varepsilon s}\,\mathrm{d}Y\right]
\end{aligned} \tag{13}$$

E_{ijkl}^H is the homogenized elastic–plastic tangent modulus in the macroscopic constitutive law. Additionally, the rates of macroscopic void volume fraction (f) and plastic work (W_p) are defined as

$$\dot{\bar{f}} = \frac{1}{Y}\int_Y \dot{f}^\varepsilon\,\mathrm{d}Y, \quad \dot{W}_p = \frac{1}{Y}\int_Y \sigma_{ij}^\varepsilon \dot{e}_{ij}^{\varepsilon p}\,\mathrm{d}Y \tag{14}$$

where $\mathbf{e}^{\varepsilon p}$ is the microscopic plastic strain in the RVE. For plane strain problems, components of E_{ijkl}^H can be obtained by averaging stress increments in response to three separate boundary value problems for the RVE. Periodic conditions $u_i(\mathbf{x},\mathbf{y}) = u_i(\mathbf{x},\mathbf{y} + k\mathbf{l_Y})\ \forall k = 1,2,\ldots$ are imposed on the boundary, where ($\mathbf{l_Y}$) correspond to the dimension vector of the RVE. Boundary value problems of the RVE are then solved with three separate imposed unit macroscopic strains increments $\Delta\bar{e}_{ij}$ in Eq. (10). Details of this process can be found in Ghosh et al. (1996, 2001, 2007) and Raghavan and Ghosh (2005).

2.3. Identification of the RVE size for homogenization

The size of the microstructural RVE is an important parameter in the determination of effective material properties. Identification of the appropriate RVE that locally represents the effect of the microstructure in an average sense is an essential part of homogenization. It is of interest to identify statistically equivalent RVEs or SERVEs that may be used for homogenization. A SERVE is the smallest volume element of the microstructure exhibiting the following characteristics.

- Effective constitutive material properties for the SERVE should equal those for the entire microstructure, within a prescribed tolerance.
- The SERVE should not depend on the location in the microstructure from where it is extracted.

Pyrz (1994) has introduced the pair distribution function $g(r)$ and the marked correlation function $M(r)$ to characterize microstructures based on inter-inclusion distances. While $g(r)$ provides a univariate characterization in terms of geometry, $M(r)$ results in a multivariate characterization. Every inclusion is marked by an appropriate descriptor to display the effect of a property that varies with the geometrical arrangement of inclusions. Marked correlation functions correlate any chosen field variable like stress, strain or their dependent functions, with the morphology of the microstructure. It is expressed as

$$M(r) = \frac{h(r)}{g(r)} \quad \text{where } h(r) = \frac{1}{2\pi r}\frac{\mathrm{d}H(r)}{\mathrm{d}r} \text{ and } H(r) = \frac{1}{m^2}\frac{A}{N^2}\sum_i^N \sum_{k=1}^{k_i} m_i m_k(r) \tag{15}$$

Here, m_i is a mark associated with the i-th inclusion. A high value of $M(r)$ indicates strong correlation between entities in the microstructure. As discussed in Ghosh et al. (1997a, b), the size of the RVE corresponds to the region of influence in the microstructure and $M(r)$ provides a good estimate of this size.

Numerical experiments have been conducted with various marked correlation functions in this study. These experiments indicate that when $M(r)$ is calculated from the micromechanical plastic work W_p in each Voronoi cell (see Fig. 1(c)), it is independent of the loading conditions. Consequently, the plastic work based $M_{wp}(r)$ is calculated for the scanning electron micrograph shown in Fig. 1(a, b) for three different loading conditions, viz. simple tension, bi-axial tension and shear, respectively. The values of $M(r)$ show very little dependence on the value of the overall strain state. The $M(r)$ function for the different load conditions are plotted as functions of r in Fig. 2(a). It stabilizes to near-unity values (within a tolerance of ~4%) at a radius of convergence r_p. For $r > r_p$, $M(r) \to 1$ and the local morphology ceases to have any significant influence on the state variables beyond this characteristic distance. The radius r_p corresponds to a local correlation length that provides an estimate for the RVE size. The correlation length r_p is plotted as a function of the equivalent strain e_{eq} for the different load conditions in Fig. 2(b). The value of r_p does not change much with increasing strain and it converges to the same value 30 μm. Consequently, a window size of $\sim 2r_p$ or 60 μm is considered as the size of the SERVE for the microstructure in Fig. 1(a, b).

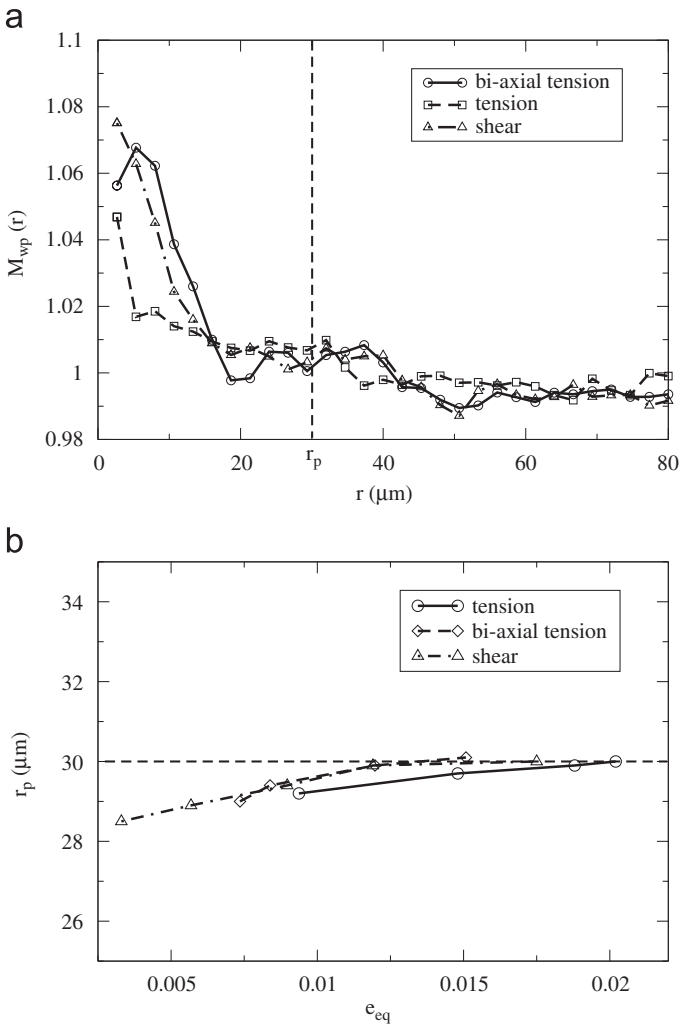

Fig. 2. (a) Plots of $M(r)$ for different loading conditions; (b) evolution of r_p for different loading conditions.

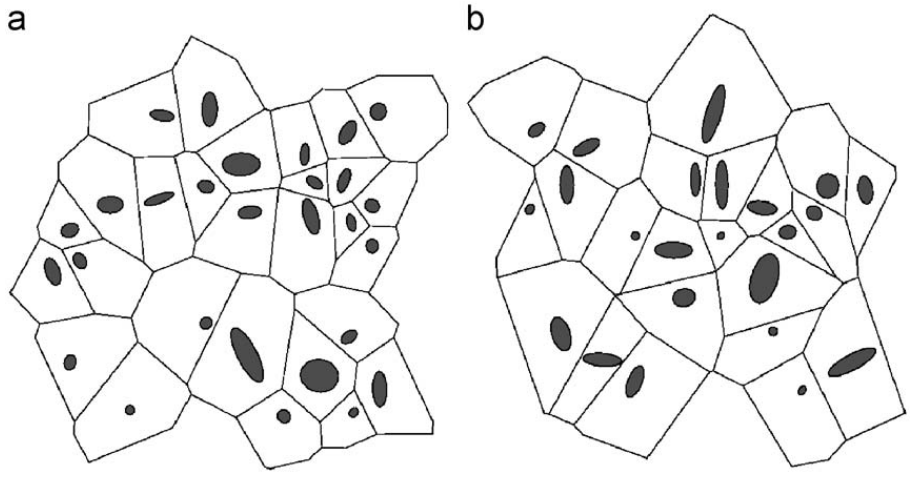

Fig. 3. (a) Window (A) with periodic boundary; (b) window (B) with periodic boundary.

Location independence of the 60 μm SERVE size is also verified by extracting RVEs from two locations A and B in the microstructure of Fig. 1(a). The boundaries of the RVEs are created by periodically repeating the position of inclusions in the x- and y-directions, followed by tessellation. This is shown in Fig. 3. The local area fraction of inclusions in the windows A and B are 6.072% and 6.090%, respectively, in comparison with 6.078% for the entire microstructure. Homogenization of the results of micromechanical LE-VCFEM analyses is performed for these two RVEs, as well as for the whole microstructure of Fig. 1 under different loading conditions. Both intact and cracking inclusions are considered in the analyses. The

homogenized stress–strain responses for the intact and cracking inclusions are plotted in Fig. 4(a, b). The results for the two RVEs match well with those for the entire microstructure. This justifies the choice of r_p in determining the SERVE.

2.4. Estimating the characteristic length for the macroscopic non-local GTN model

The material characteristic length scale L in Eq. (8) of the GTN constitutive model is a parameter that controls the effective zone of non-local weighting of $\dot{f}$. A marked correlation function $M_{AF}(r)$, based on the local inclusion area fraction in

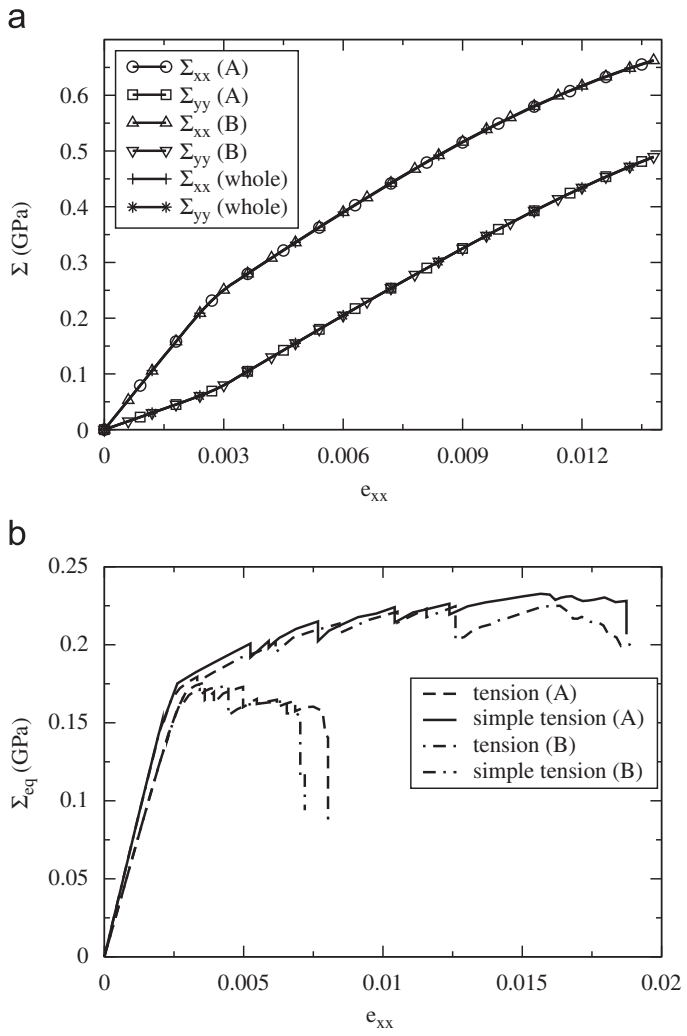

Fig. 4. Comparisons of macroscopic stress–strain response: (a) without inclusion cracking and (b) with inclusion cracking.

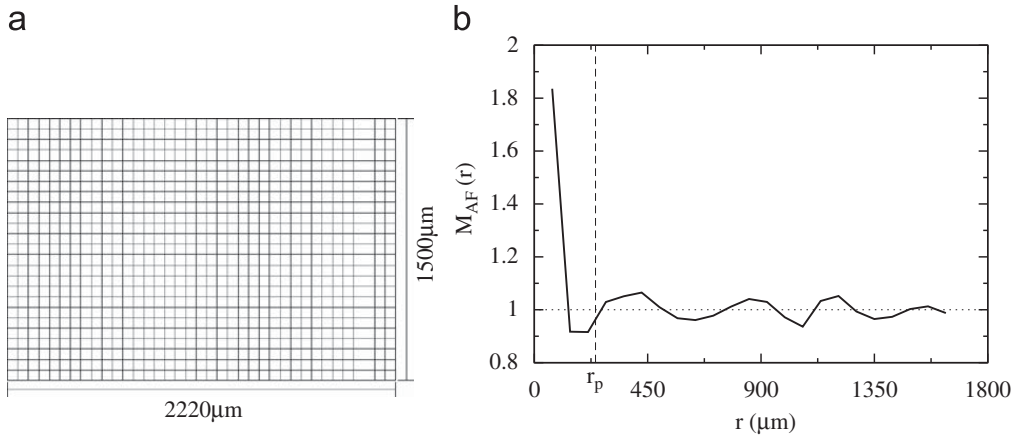

Fig. 5. (a) Microstructure of a cast aluminum A-319 micrograph with an uniform grid; (b) corresponding plot of $M(r)-r$.

the microstructure, is chosen to estimate L for the continuum plasticity-damage model. The local area fraction is a geometric parameter that significantly affects the local stress and strain distributions and hence the local material constitutive response. Thus the correlation length for the local inclusion area fraction is assumed to represent the 'non-local' characteristic length scale in the GTN model. $M_{AF}(r)$ is evaluated for the $2220\,\mu m \times 1500\,\mu m$ micrograph of a cast aluminum alloy, shown in Fig. 5(a). The local area fraction is estimated by dividing the entire micrograph into 925 square blocks of size $60\,\mu m \times 60\,\mu m$ each, which corresponds to the RVE size determined in Section 2.3. The average area fraction of inclusions is evaluated in each of these blocks. The function $h(r)$ is derived from $H(r)$ in Eq. (15) for which, $N = 925$ and $A = 2220\,\mu m \times 1500\,\mu m = 3.33 \times 10^6\,\mu m^2$. The $M_{AF}(r)-r$ plot in Fig. 5(b) indicates stabilization at $r_p \approx 240\,\mu m$. This value is approximately 4 times the size of the SERVE, determined in Section 2.3. The material characteristic length used is $L = 240\,\mu m$ for the macroscopic non-local GTN model.

3. Development of homogenization-based continuum plasticity-damage model framework

The homogenization-based continuum plasticity-damage model is developed using the tools discussed in Section 2. The HCPD model is for plane strain analysis, since it is created from plane strain micromechanical analysis by LE-VCFEM. An anisotropic Gurson–Tvergaard–Needleman model framework is adopted following developments in Liao et al. (1997), Wang et al. (2004), Grange et al. (2000) and Benzerga et al. (2004). The anisotropic yield function for porous ductile materials containing inclusions is expressed in terms of the deviatoric and hydrostatic components of stress and the void volume fraction as

$$\bar{\Phi} = \frac{\Sigma_{eq}^2}{Y_f^2(W_p)} + 2Q_1 f \cosh\left(\frac{3Q_2}{2}\frac{\Sigma^{hyd}}{Y_f(W_p)}\right) - 1 - (Q_1 f)^2 = 0 \tag{16}$$

Σ_{eq} and Σ^{hyd} are the homogenized equivalent and hydrostatic stresses, respectively, and f is the averaged void volume fraction. Y_f is the homogenized flow stress in shear of the heterogeneous material without voids that is a function of the macroscopic plastic work W_p. Eq. (16) reflects anisotropy from two sources, viz. (i) arbitrary dispersion of brittle inclusions in the matrix and (ii) evolution of voids in the microstructure. Anisotropy due to inclusions in the matrix is accounted for through the expression of the equivalent stress Σ_{eq}. For plane strain problems, this is expressed using the 2D anisotropic yield function in Hill (1948) as

$$\Sigma_{eq}^2 = F(\Sigma_{yy} - \Sigma_{zz})^2 + G(\Sigma_{zz} - \Sigma_{xx})^2 + H(\Sigma_{xx} - \Sigma_{yy})^2 + C\Sigma_{xy}^2 \tag{17}$$

The stress components are with respect to the principal axes of material anisotropy. The anisotropic parameters F, G, H and C are calibrated by homogenization of LE-VCFEM micromechanical analyses without void evolution. It will be shown in Section 3.1.1 that these parameters are not constant, but evolve with increasing plastic flow due to the presence of heterogeneities. The corresponding effective plastic strain ($\bar{e}^p$) is written as

$$\dot{\bar{e}}^p = \sqrt{\frac{F(\dot{e}_{xx}^p)^2 + G(\dot{e}_{yy}^p)^2 + H(\dot{e}_{zz}^p)^2}{FH + GH + FG} + \frac{2(\dot{e}_{xy}^p)^2}{C}} \tag{18}$$

Here e_{ij}^p are components of the macroscopic plastic strain that may be evaluated from an associated flow rule for hardening materials i.e. $\dot{e}_{ij}^p = \dot{\lambda}\partial\bar{\Phi}/\partial\Sigma_{ij}$. The parameters Q_1 and Q_2 are associated with the hydrostatic stress and calibrated from micromechanical analysis with void evolution. The homogenized void growth law is identical to Eq. (3), while a novel model for macroscopic void nucleation is developed in Section 3.3.

3.1. Specific characteristics of the anisotropic HCPD model

3.1.1. Evolution of anisotropic parameters

Studies on anisotropic damage-plasticity models, e.g. in Liao et al. (1997), Wang et al. (2004) and Benzerga et al. (2004), assume constant plasticity parameters that do not evolve with plastic flow. To verify whether constant parameters in the homogenized GTN model can produce good agreement with results of micromechanical analysis, numerical tests are conducted for a 20-inclusion RVE (shown in the inset of Fig. 6) under the following loading conditions:

(1) Simple shear test: $e_{xx} : e_{yy} : e_{xy} = 0 : 0 : 1$.
(2) Tension test with constrained transverse strain: $e_{xx} : e_{yy} : e_{xy} = 1 : 0 : 0$.
(3) Biaxial tension test: $e_{xx} : e_{yy} : e_{xy} = 1 : 1 : 0$.

The anisotropic parameters are calibrated using the algorithm described in Section 3.2. During plastic loading, the equivalent stress Σ_{eq} in Eq. (17) equals the flow stress $Y_f(W_p)$ that is a function of the plastic work only. Consequently, plots of the equivalent stress as functions of plastic work are expected to be independent of the load history. Fig. 6(a) shows the evolution of equivalent stress with plastic work, obtained with constant values of F, G, H in the expression (17). These parameters are calibrated for $W_p = 0.0045\,GPa$. The figure shows considerable difference in $\Sigma_{eq}-W_p$ response for the

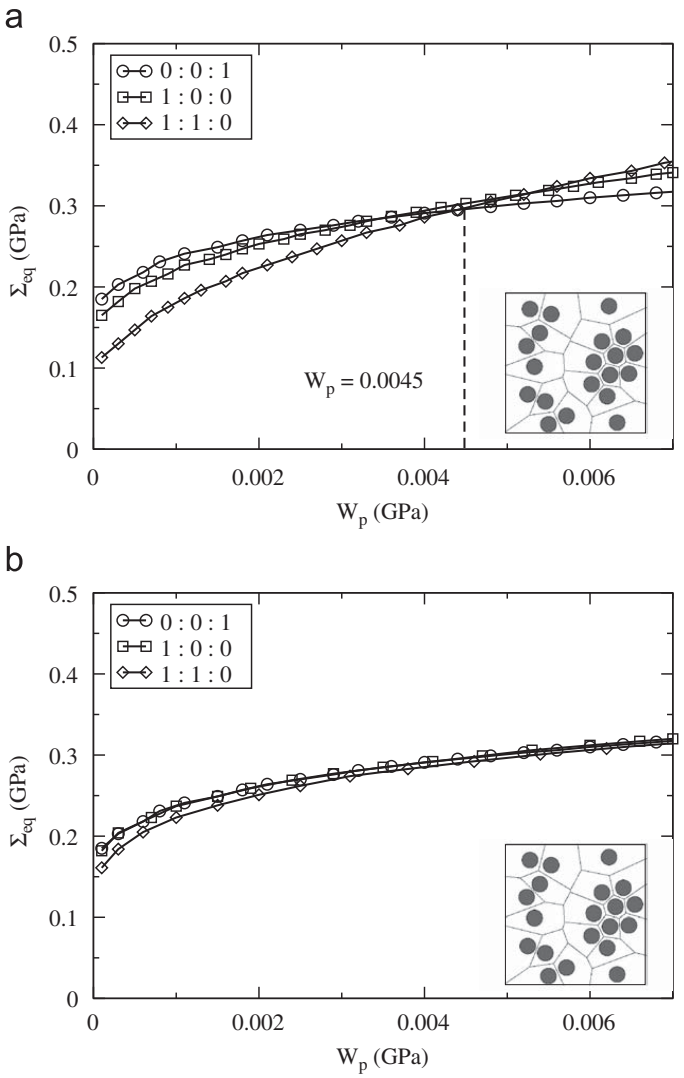

Fig. 6. Equivalent stress-plastic work responses, obtained by: (a) assuming constant anisotropy parameters and (b) using evolving anisotropy parameters.

different loading cases. They match only at the calibrating $W_p = 0.0045$ GPa. Next, the anisotropy parameters are assumed to evolve with W_p by calibrating them with evolving W_p. The corresponding $\Sigma_{eq}-W_p$ response is plotted in Fig. 6(b). The difference between the curves for different loading conditions drastically reduces for the entire interval of plastic work considered. This example establishes the need for the anisotropy parameters to be functions of the evolving plastic work.

When calibrated from the results of homogenized micromechanical analyses described in Section 3.2, the parameters exhibit significant change with evolving plastic deformation. For example, parameters F, G, H in the HCPD model of Eq. (16) are plotted as functions of the plastic work W_p in Figs. 10 and 11 for three different RVEs. Two of the RVEs have a circular inclusion of volume fractions $V_f = 1\%$ and 20%, respectively, while the third RVE contains an elliptical inclusion. For the circular inclusions, $F = G$. The figures exhibit significant effects of both morphology and size on the evolution of parameters. The plots exhibit a nonlinear dependence of F, G, H on W_p. This dependence reduces sharply with decreasing volume fraction, and the parameters approach constant values of 0.5 at the $V_f = 0$ limit. These are the values for the isotropic matrix material.

3.1.2. *Representing the GTN model in material principal coordinate system*

Material anisotropy is determined not only by the morphology of the microstructure, e.g. size, shape and distribution of heterogeneities, but also by the evolution of plastic deformation and damage. It is important to account for the history of deformation and loading in the anisotropic *HCPD* model. This is facilitated by expressing the *HCPD* model in reference to an evolving material principal coordinate system. To test the effectiveness of this hypothesis, micromechanical analysis of an RVE consisting of a circular fiber of $V_f = 20\%$ in square matrix is conducted with an imposed non-proportional load history. A tensile strain history ($e_{xx} : e_{yy} : e_{xy} = 1 : 0 : 0$) is applied till $e_{xx} = 0.005$. This is followed by a shear strain ($e_{xx} : e_{yy} : e_{xy} = 0 : 0 : 1$) till $e_{xy} = 0.011$. Results generated by the *HCPD* model are compared with the homogenized micromechanical analysis results in Fig. 7. The first part of the loading, corresponding to proportional loading, shows

good agreement. However, in a fixed reference coordinate system, error accumulates with additional straining in the non-proportional second half of the loading. Stress and strain components in the anisotropic yield function of Eq. (16) are consequently referred to an evolving material principal coordinate system. The material is assumed to remain orthotropic

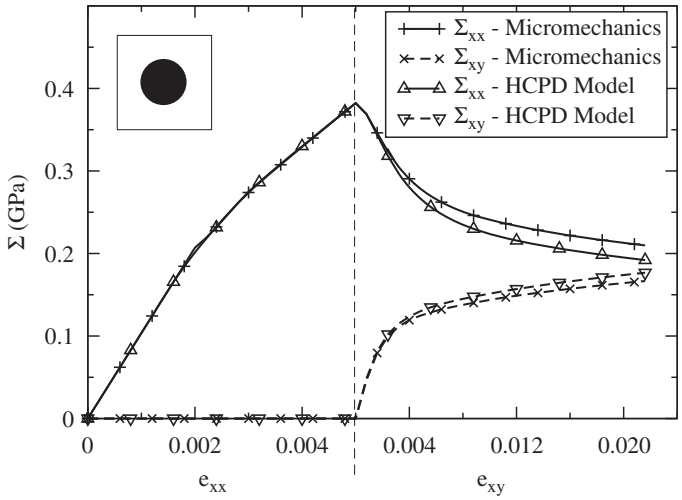

Fig. 7. Comparison of stress–strain data from HCPD model analysis in a fixed coordinate system, with that from micromechanical analysis for a problem with non-proportional load history.

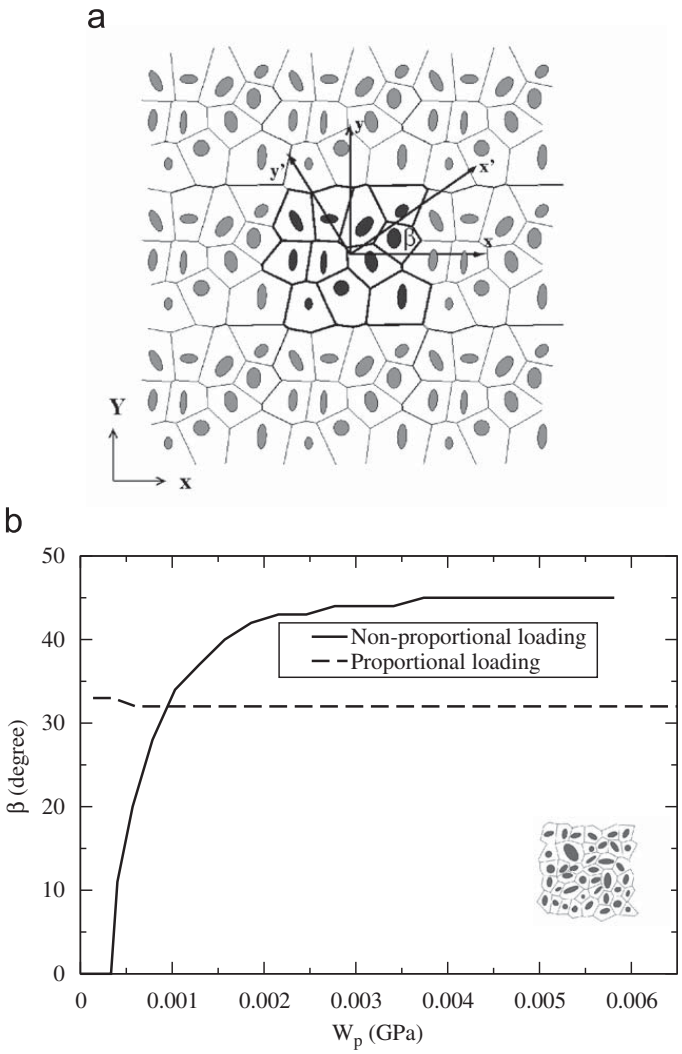

Fig. 8. (a) A periodically repeated RVE showing principal axes of material anisotropy; (b) evolution of the principal axes angle for proportional and non-proportional loads on the RVE with 40 randomly distributed inclusions.

in this system throughout the deformation process. The angle β shown in Fig. 8(a) corresponds to principal axes of anisotropy for plane strain analysis. In every load step, β is determined from the condition that the transformed tangent modulus $(E^{\tan}_{ijkl})'$ in this system corresponds to orthotropy, i.e. terms coupling normal and shear components of the tangent modulus are equal to zero, i.e.

$$(E^{\tan}_{1112})' = (E^{\tan}_{2212})' = (E^{\tan}_{3312})' = 0 \tag{19}$$

where $(E^{\tan}_{ijkl})' = Q_{im}Q_{jn}Q_{kp}Q_{lq}E^{\tan}_{mnpq}$ and

$$[\mathbf{Q}] = \begin{bmatrix} \cos\beta & \sin\beta & 0 \\ -\sin\beta & \cos\beta & 0 \\ 0 & 0 & 1 \end{bmatrix}$$

Anisotropic parameters are calibrated next with respect to this principal coordinate system. The evolution of the principal material-damage axes is shown in Fig. 8(b) for two different loading conditions on an RVE with 40 randomly distributed inclusions. The RVE is shown in the inset of the figure. One of the loadings is proportional, by a strain ratio $e_{xx} : e_{yy} : e_{xy} = 1 : 0 : 2$. The other is a non-proportional loading in which a x-direction tension load is followed by a simple shear as described before. The principal directions do not evolve much for the proportional loading case. For the non-proportional loading case, the principal axes angle remains relatively unchanged during the tension phase but increases nonlinearly with shear before finally reaching a saturation condition. Plots of the evolution for other microstructures (not shown here) have also exhibited a similar behavior.

3.2. Evaluation of anisotropic constitutive parameters in the HCPD model

3.2.1. $Y_f(W_p)$ and C in Eq. (17)

Since $Y_f(W_p)$ is the flow stress in shear, an LE-VCFEM-based micromechanical RVE analysis is conducted for shear straining, with $e_{xx} = e_{yy} = 0$, $e_{xy} \neq 0$. The matrix material is assumed to be void free and no inclusion fragmentation is

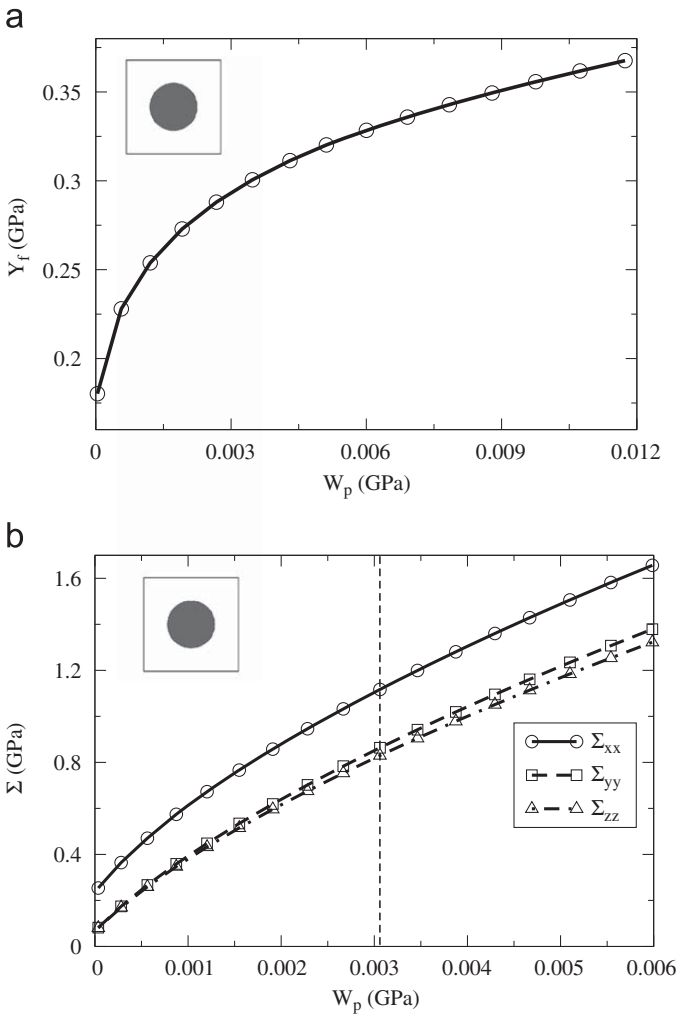

Fig. 9. (a) Yield stress for shear loading and (b) homogenized stresses for tensile loading, plotted as functions of macroscopic plastic work.

allowed. Micromechanical analysis is followed by homogenization, in which the macroscopic plastic work, stresses and strains are evaluated from the microstructural variables using Eqs. (13) and (14). For pure shear loading, $\Sigma_{xx} = \Sigma_{yy} = \Sigma_{zz} = 0$ and $\Sigma_{xy} \neq 0$. The parameter C in Eq. (17) is set to 3 to make $Y_f(W_p) = \sqrt{3}\Sigma_{xy}$. The flow stress Y_f is plotted as a function of W_p in Fig. 9(a).

3.2.2. Parameters F, G and H in Eq. (17)

(1) For a given RVE, numerical simulations are performed using LE-VCFEM for different loading conditions, followed by homogenization. No void evolution or inclusion cracking is allowed in these simulations. Loading conditions are prescribed with different macroscopic strain paths. A total of 13 numerical experiments, corresponding to a range of different strain ratios (paths) $e_{xx} : e_{yy} : e_{xy}$ are performed. The strain paths are: $1:0:0$, $0:1:0$, $2:1:0$, $1:2:0$, $1:1:0$, $1:0:1$, $0:1:1$, $1:0:2$, $0:1:2$, $2:1:1$, $1:2:1$, $1:1:1$, $1:1:2$. At the end of each strain increment, the tangent stiffness $E^{\tan}_{ijkl}$ is evaluated and subsequently the principal axes of anisotropy are determined from Eq. (19). Macroscopic stresses and plastic work in the principal coordinate system are obtained from Eqs. (13) for each load step. The macroscopic stress components in the principal axes of anisotropy are plotted as functions of W_p in Fig. 9(b), for the strain ratio 1:0:0.

(2) For a given value of W_p, $Y_f(W_p)$ is obtained from the plots such as Fig. 9(a), and the stress components from plots such as in Fig. 9(b). This is done for all the load histories. The plastic work dependent parameters $F(W_p), G(W_p), H(W_p)$ are then evaluated by least square minimization of the function (17) as

$$\min_{F,G,H} \sum_{i=1}^{N} [F(\Sigma^i_{yy} - \Sigma^i_{zz})^2 + G(\Sigma^i_{zz} - \Sigma^i_{xx})^2 + H(\Sigma^i_{xx} - \Sigma^i_{yy})^2 + C(\Sigma^i_{xy})^2 - (Y^i_f)^2]^2 \tag{20}$$

Here N is the number of data points corresponding to all the 13 different loading paths, for a given value of W_p. The parameters F, G, H are solved by an iterative algorithm with $C = 3$. The step is repeated for different values of W_p to obtain the W_p dependence of the parameters. Figs. 10–14 depict the evolution of F, G, H for five different RVEs shown in the inset. The RVEs all have inclusion volume fraction $V_f = 20\%$. While F and G reduce nonlinearly with W_p, H increases with W_p. For the RVEs in Figs. 10, 12 and 14, symmetry of inclusion shapes and dispersions render the pre-damage response relatively isotropic and hence $F \approx G$. However, the shapes and dispersions in the microstructures of Figs. 11 and 13 make $F \neq G$. While the initial values of the parameters are similar for many of the RVEs, their rates of change with increasing W_p are different for the different microstructures.

3.2.3. Parameters Q_1 and Q_2 in Eq. (16)

A set of micromechanical problems, now with void evolution, is solved with subsequent RVE homogenization for evaluating the coefficients Q_1 and Q_2 in Eq. (16). The following sequence of analyses are undertaken for this objective.

(1) An LE-VCFEM simulation of the RVE is conducted with an applied macroscopic shear strain for plastic deformation and void evolution. The corresponding macroscopic stress and averaged void volume fraction are evaluated and plotted as functions of the averaged matrix plastic work, whose rate is defined in Eq. (14). Since the normal stresses $\Sigma_{xx} = \Sigma_{yy} =$

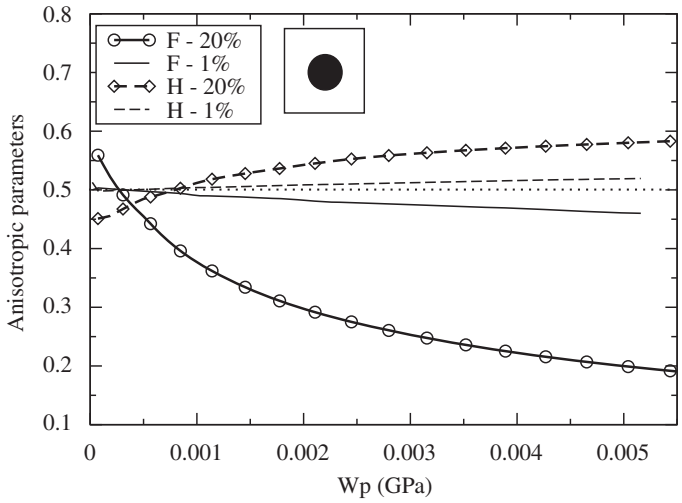

Fig. 10. Evolution of the anisotropy parameters F, H for RVE with one circular inclusion.

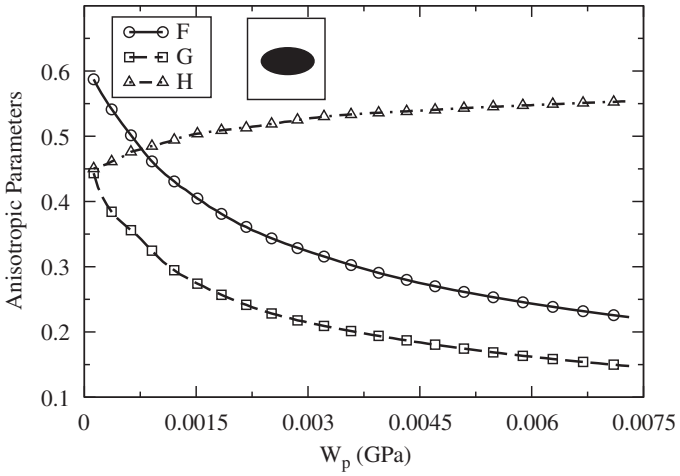

Fig. 11. Evolution of the anisotropy parameters F, G, H for RVE with one elliptical inclusion.

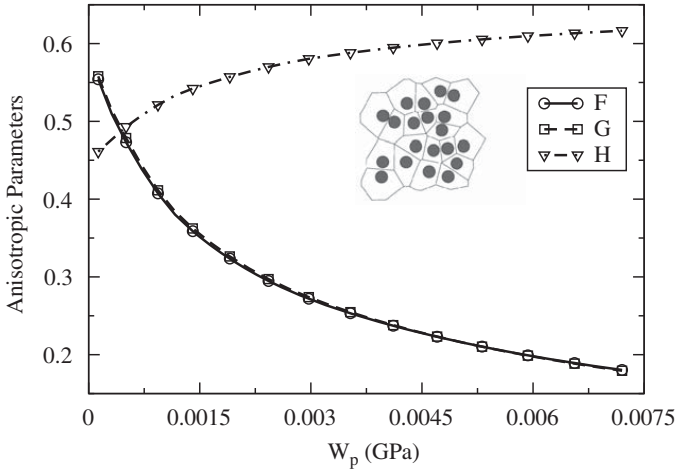

Fig. 12. Evolution of anisotropy parameters F, G, H for RVE with 20 circular inclusions.

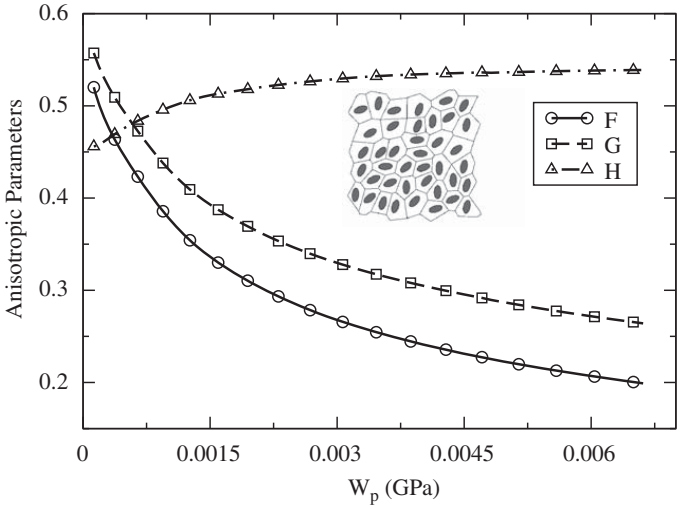

Fig. 13. Evolution of anisotropy parameters F, G, H for RVE with 40 elliptical inclusions.

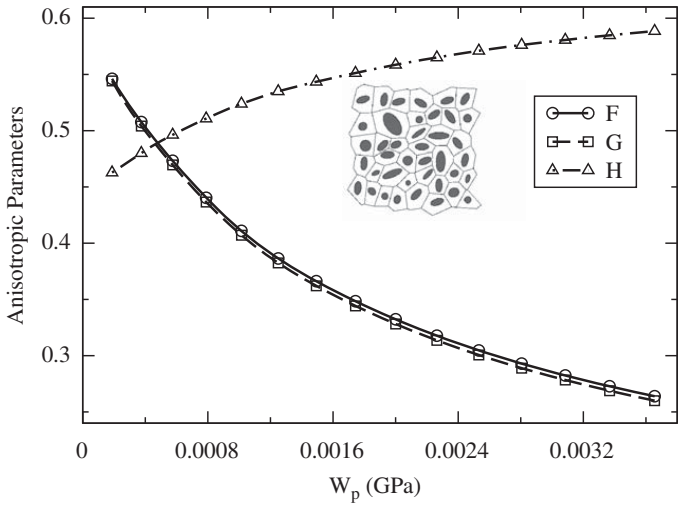

Fig. 14. Evolution of anisotropy parameters F, G, H for RVE with 40 inclusions of random elliptical shapes.

Table 1
Mean and standard deviation of calibrated parameters Q_1 and Q_2 for different RVEs.

	Mean of Q_1	Standard dev. of Q_1	Mean of Q_2	Standard dev. of Q_2
RVE 1	1.84	0.0079	1.03	0.0185
RVE 2	1.84	0.0059	1.02	0.0087
RVE 3	1.92	0.0098	1.04	0.0232
RVE 4	1.87	0.0157	1.06	0.0205
RVE 5	1.72	0.0894	1.09	0.0316

$\Sigma_{zz} = 0$ for this loading, and also the hydrostatic part of plastic strain $\partial\bar{\Phi}/\partial\Sigma_{kk} = 0$, the void volume fraction does not change, i.e. $f = f_0$. The parameter Q_1 can be solved from the quadratic equation (16) as

$$Q_1 = \frac{1}{f_0}\left(1 - \frac{\sqrt{3}\Sigma_{xy}}{Y_f}\right) \tag{21}$$

(2) The same set of numerical experiments as in Section 3.2.2 is again performed for the microstructural RVEs with non-zero, evolving void volume fractions. Again, assuming sole dependence on W_p, the parameter $Q_2(W_p)$ is evaluated from known values of F, G, H and Q_1 by solving the minimization problem

$$\min_{Q_2} \sum_{i=1}^{N} \left[\frac{\Sigma_{eq}^2}{Y_f^2} + 2Q_1 f \cosh\left(\frac{3Q_2}{2}\frac{\Sigma^{hyd}}{Y_f}\right) - 1 - (Q_1 f)^2\right]^2 \tag{22}$$

The calibrated values of Q_1 and Q_2 for the different RVEs exhibit only minimal dependence on plastic work. The mean and standard deviation of Q_1 and Q_2 for the five RVEs of Figs. 10–14 are listed in Table 1. The standard deviations of Q_1 and Q_2 are very small compared to the mean values, and hence Q_1 and Q_2 for each RVE are taken as constants in the analyses.

The parameters Q_1 and Q_2 depend on the RVE they are calibrated from. The Q_1 values are quite different from the value ($q_1 = 1.5$) in the pure matrix material. The difference is attributed to the effect of the inclusion volume fraction V_f. Q_1 is found to be approximately inversely proportional to the matrix volume fraction and is expressed as

$$Q_1 = \frac{q_1}{1 - V_f} \tag{23}$$

This expression is further corroborated by a comparison of the functional dependence of Q_1 from this equation with that derived from micromechanical analyses of RVEs containing a single inclusion of various volume fractions. The results are depicted in Fig. 15. This sensitivity may be explained by the increase of the porosity in the matrix at the microscale when the volume fraction of inclusions is increased for a constant macroscopic void volume fraction. On the other hand, Q_2 is quite close to the matrix material value ($q_2 = 1$) and is taken as $Q_2 = 1$ in subsequent simulations.

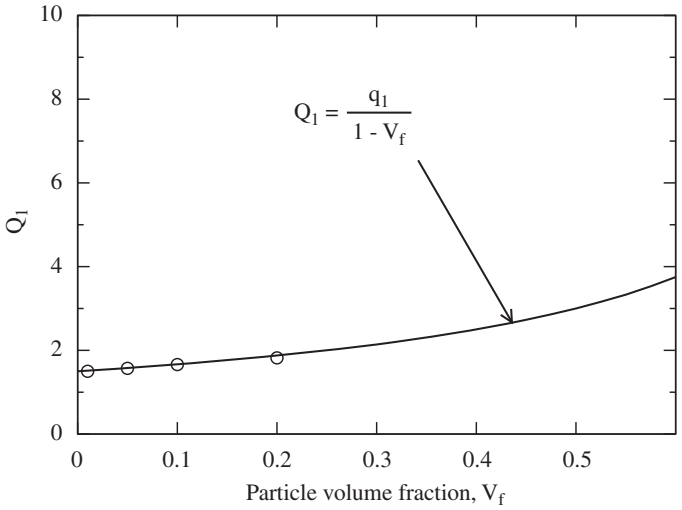

Fig. 15. Dependence of Q_1 on inclusion volume fraction by micromechanics and the proposed formula.

3.3. Void nucleation in the HCPD model

Microstructural damage initiation can occur by inclusion fragmentation accompanied by matrix void evolution. This manifests as void nucleation in the macroscopic *HCPD* model. As an example, the averaged equivalent stress–strain responses for a microstructure with 20 inclusions are shown in Fig. 16(a). The two plots, corresponding to tension tests in the x- and y-directions, respectively, are considerably different. Contour plots of the void volume fraction along with cracked inclusions are shown in Fig. 17. For tension in the x-direction, cracks localize in one of the inclusion clusters, while they are more diffused for the y-direction test. Each time an inclusion cracks, the stress–strain response curve experiences an instantaneous drop. It is difficult to represent every drop individually in the macroscopic *HCPD* model. Hence, a continuous and smooth response curve, projecting the overall loss of load carrying capacity as a consequence of inclusion cracking, is desirable in this continuum void nucleation model.

The relations in Eqs. (4) are commonly used plastic strain controlled void nucleation criteria. However, these equations are unable to generate the necessary anisotropy in stress–strain response for different loading conditions. Results of tension test simulations in the x- and y-directions with the nucleation equations (4) are shown in Fig. 16(b). Nucleation parameters used are $e_N = 0.045$, $s_N = 0.05$ and $f_N = 0.05$. The difference in response for the two tests is significantly smaller than the micromechanical results of Fig. 16(a). This is because the difference in the equivalent plastic strain for the two loadings is very small, even with material anisotropy. This observation calls for a modified macroscopic void nucleation criterion in the presence of dispersed heterogeneities.

The void nucleation model is based on a two-parameter Weibull statistics-based fracture probability $\bar{P}_{fr}$, which dictates inclusion cracking in the microstructure in Eq. (9). The probability function is expressed in terms of the inclusion volume and a strain measure as

$$\bar{P}_{fr}(v,\hat{e}) = 1 - \exp\left[-\frac{v}{v_0}\left(\frac{\hat{e}}{e_0}\right)^m\right] \tag{24}$$

where e_0 and m are Weibull parameters to be calibrated, v_0 is the average volume of inclusions, $\hat{e}$ is a prescribed function of strain and v is the inclusion volume. The function $\hat{e}$ is expressed in terms of 'strain invariant-like' functions I_1 and I_2 for anisotropy as

$$\hat{e} = I_1 + I_2 \quad \text{where } I_1 = Ae_1 + Be_2 + Ce_3 \text{ and } I_2 = D(e_2 - e_3)^2 + E(e_3 - e_1)^2 + F(e_1 - e_2)^2 \tag{25}$$

Here e_1, e_2 and e_3 are principal strains, and A, B, C, D, E, F are constant parameters calibrated from micromechanical analysis of deformation with inclusion fragmentation. Similar fracture probabilities have been suggested in Llorca and Gonzalez (1998). The fraction of cracked inclusions ρ may be expressed in terms of the probability density of inclusion size $p(v)$ and $\bar{P}_{fr}(v,\hat{e})$ as

$$\rho(\hat{e}) = \int_0^\infty p(v)\bar{P}_{fr}(v,\hat{e})\,\mathrm{d}v \tag{26}$$

If all the inclusions in the microstructure have the same size, i.e. $p(v) = 1$, the fractured inclusion fraction becomes

$$\rho(\hat{e}) = 1 - \exp\left[-\left(\frac{\hat{e}}{e_0}\right)^m\right] \tag{27}$$

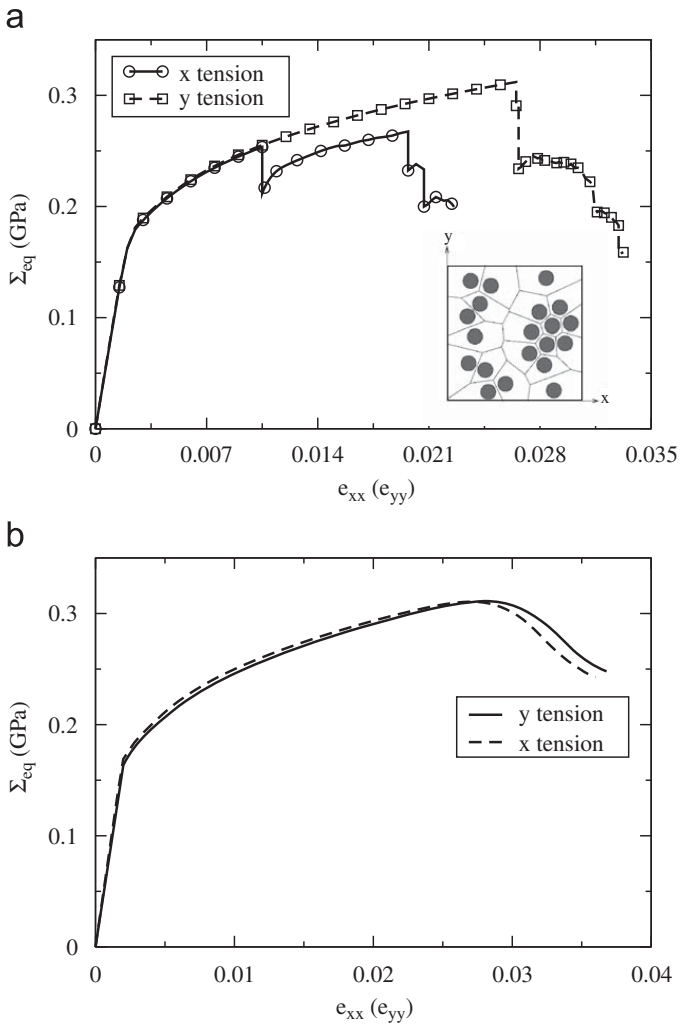

Fig. 16. (a) Equivalent stress–strain response: (a) obtained by averaging micromechanical analysis, showing stress drops due to cracked inclusions and (b) using the macroscopic plastic strain controlled void nucleation equation (4).

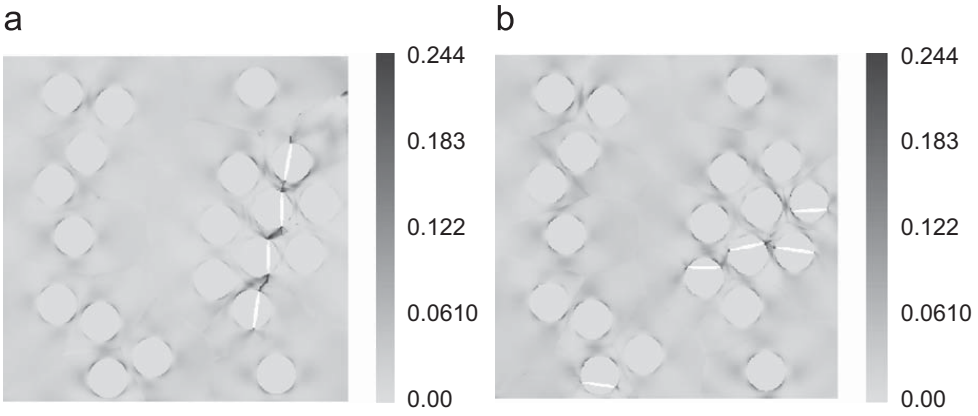

Fig. 17. Contour plots of void volume fraction showing cracked inclusions in tension test along: (a) *x*- and (b) *y*-directions.

For inclusions of different sizes in the real micrographs of Fig. 1, the size distribution is determined to be of the type

$$p(v) = \frac{4v}{v_0^2}\exp\left\{\frac{-2v}{v_0}\right\} \tag{28}$$

This is corroborated by probability density observations in Llorca and Gonzalez (1998). Correspondingly, the fractured inclusion fraction is derived from Eq. (26) to be

$$\rho(\hat{e}) = 1 - \frac{1}{\left[1 + \frac{1}{2}\left(\frac{\hat{e}}{e_0}\right)^m\right]^2} \tag{29}$$

A comparison of the cracked inclusion fraction by Eqs. (27) and (29) for $m = 3$ and $\varepsilon_0 = 0.0082$ is plotted in Fig. 18. For low and high strains, these two curves almost overlap with each other. The difference is, however, pronounced for intermediate strains.

Finally, the void nucleation rate for the *HCPD* model is expressed as

$$\dot{f}_{nucleation} = A(\hat{e})\dot{\hat{e}} = V_p \frac{d\rho(\hat{e})}{d\hat{e}}\dot{\hat{e}} \tag{30}$$

where V_p is a parameter that can be calibrated from the volume fraction of cracked inclusions at given strain.

3.3.1. Calibration of parameters in the void nucleation model

A total of five LE-VCFEM simulations along with the *HCPD* model analyses are conducted for calibrating parameters in Eq. (25). The tests are with different loading conditions, viz.:

(1) Tension tests in the x- and y-directions, with zero transverse strains.
(2) Simple tension tests in the x- and y-directions.
(3) Biaxial tension test.

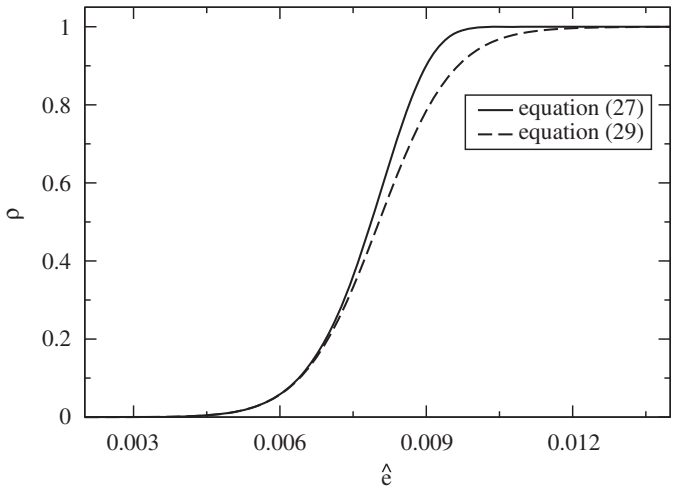

Fig. 18. Comparison of Eqs. (27) and (29) for same m and ε_0.

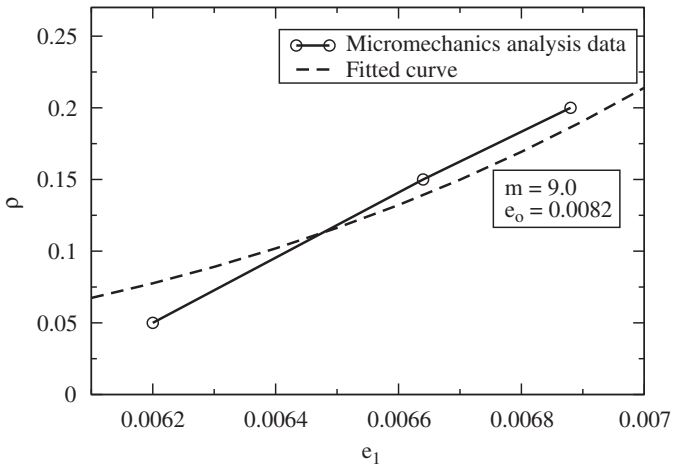

Fig. 19. Fraction of fractured inclusions as a function of the overall strain from LE-VCFEM analysis and the nucleation model.

The x-direction constrained tension test (1) is used as a reference loading. The corresponding fractured inclusion fraction ρ is plotted as a function of the principal strain e_1 in Fig. 19. The three data points in this figure correspond to the fraction of fractured inclusions at certain strains.

Parameters e_0 and m are calibrated to fit the micromechanical analysis data in Fig. 19. The fitted curve is used as a reference to calibrate the parameters A, B, C, D, E and F. The fraction of cracked inclusions in the micromechanical simulations are recorded at different values of strain components. For each value of ρ in the different loading cases, $\hat{e}$ is obtained from Fig. 19. The parameters are calibrated using the least square method to minimize the difference between micromechanical and HCPD-simulation results:

$$\min_{A,B,C,D,E,F} \sum_{i=1}^{N} \sum_{j=1}^{5} [I_1 + I_2 - \hat{e}]^2 \tag{31}$$

where N corresponds to all the recorded values of ρ. Subsequently the parameter V_p, which relates the volume fraction of cracked inclusions to the void nucleation rate in the HCPD model, is evaluated iteratively from several macroscopic x-direction tension test analyses.

3.4. Implementation of HCPD model in a macroscopic analysis module

The homogenization-based continuum plasticity-damage model is incorporated in macroscopic FEM codes for deformation and failure of ductile materials containing brittle inclusions. In the incremental small deformation formulation, stress increments are related to increments of strains as

$$\Delta\Sigma_{ij} = E_{ijkl}(\Delta e_{kl} - \Delta e^p_{kl}) \tag{32}$$

where E_{ijkl} is the homogenized elasticity tensor. From the associated flow rule, the components of plastic strain increment are related as

$$\begin{aligned}
\Delta e^p_{xx}\left(\frac{\partial\bar{\Phi}}{\partial\Sigma_{yy}}\right) - \Delta e^p_{yy}\left(\frac{\partial\bar{\Phi}}{\partial\Sigma_{xx}}\right) &= 0\\
\Delta e^p_{xx}\left(\frac{\partial\bar{\Phi}}{\partial\Sigma_{zz}}\right) - \Delta e^p_{zz}\left(\frac{\partial\bar{\Phi}}{\partial\Sigma_{xx}}\right) &= 0\\
\Delta e^p_{xx}\left(\frac{\partial\bar{\Phi}}{\partial\Sigma_{xy}}\right) - \Delta e^p_{xy}\left(\frac{\partial\bar{\Phi}}{\partial\Sigma_{xx}}\right) &= 0
\end{aligned} \tag{33}$$

With known increments of strains from macroscopic analysis, the set of Eq. (33), together with the yield equation (16), are solved iteratively in the material principal axes system by using the backward Euler method. This yields the stress increments in the following steps.

(1) Initialize $\Delta\Sigma_{xx}$, $\Delta\Sigma_{yy}$, $\Delta\Sigma_{zz}$ and $\Delta\Sigma_{xy}$ by using $\Delta\Sigma_{ij} = E_{ijkl}\Delta e_{kl}$.
(2) Calculate the gradient $(\partial\bar{\Phi}/\partial\Sigma_{ij})$ of yield function and solve for the increments of plastic strain Δe^p_{xx}, Δe^p_{yy}, Δe^p_{zz} and Δe^p_{xy} from Eqs. (16) and (33).
(3) Update stresses, void volume fraction and plastic work $\Delta W_p = \Sigma_{ij}\Delta e^p_{ij}$.
(4) Update all parameters and yield stresses using the updated plastic work.
(5) If $\bar{\Phi} \leqslant tol_1$ and correction to plastic strain increment $\delta e^p_{ij} \leqslant tol_2$, then update the tangent modulus and go to the next step. Otherwise continue iteration from step (2).

4. Numerical examples with the HCPD model

4.1. Validation with results of micromechanical analysis

The HCPD model is validated by comparing the results of macroscopic finite element simulations with those obtained by homogenizing the LE-VCFEM-based micromechanical solutions. The study considers a variety of different microstructural RVEs as well as different proportional and non-proportional loading conditions. The macroscopic model consists of a single bilinear QUAD4 element in the commercial code ABAQUS with one integration point. Material properties considered are:

Ductile matrix material: Young's modulus $E = 75$ GPa, Poisson's ratio $\nu = 0.22$, initial void volume fraction $f_o = 0.01$, Parameter in Eqs. (4) and (5): $f_N = 0.08$, $\varepsilon_N = 0.2$ and $s_N = 0.075$. Post-yield behavior for the matrix material without voids is expressed by the Ramberg–Osgood law $\sigma_m = \sigma_0(\varepsilon^p_m/\alpha\varepsilon_0)^{1/n}$, where ε_0 is the strain at yield ($\varepsilon_0 = \sigma_0/E$). The initial flow stress $\sigma_0 = 175$ MPa and $\alpha = \frac{3}{7}$ and strain hardening exponent $n = 4$.

Brittle reinforcing SiC inclusions: Young's modulus $E = 320$ GPa, Poisson's ratio $\nu = 0.25$.

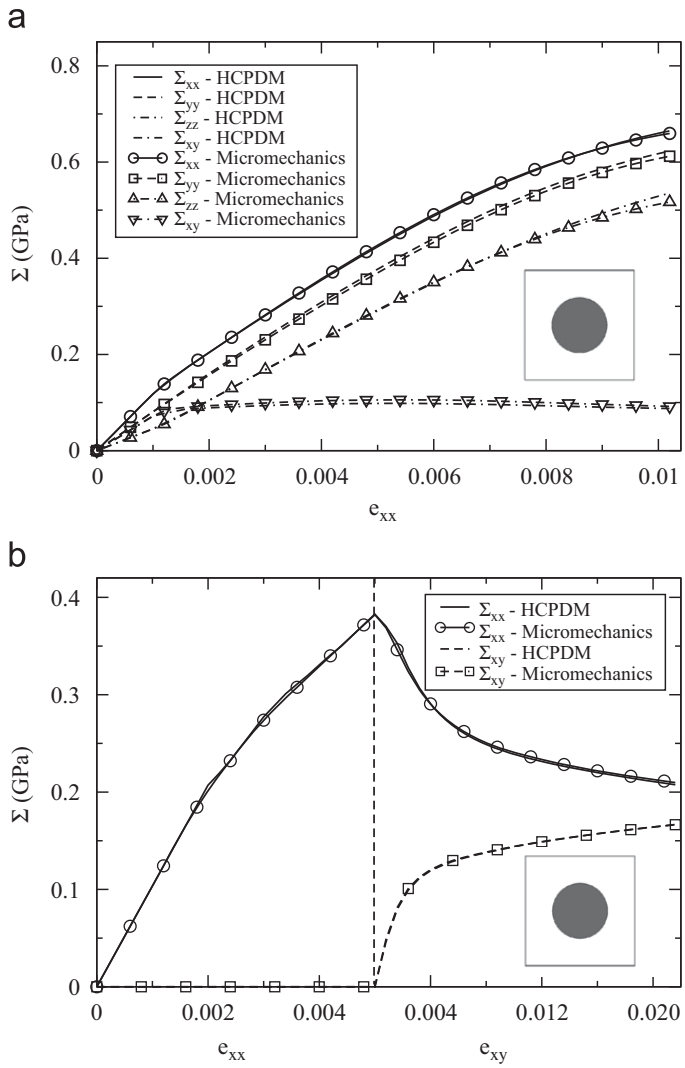

Fig. 20. Macroscopic stress–strain response by the HCPD model and homogenized micromechanical solutions for RVE (A): (a) $e_{xx} : e_{yy} : e_{xy} = 2 : 1 : 2$ and (b) non-proportional loading.

4.1.1. Analyses with different RVEs

Five different RVEs, each containing inclusions of 20% volume fraction are considered for simulation. These are described below.

(A) Square unit cell containing one circular inclusion (inset of Fig. 20).
(B) Square unit cell with an elliptical inclusion of aspect ratio $a/b = 2$ (inset of Fig. 21).
(C) Square RVE with a non-uniform dispersion of 20 identical circular inclusions (inset of Fig. 22).
(D) Square RVE with a non-uniform dispersion of 40 identical elliptical inclusions with different orientation (inset of Fig. 23).
(E) Square RVE with a non-uniform dispersion of 40 inclusions of different shapes and sizes and orientations (inset of Fig. 24).

RVE simulations are conducted for two macroscopically imposed strain paths that are different from those considered in the parameter calibration process. The results of the HCPD model simulations are compared with those by averaged micromechanical analyses. The first loading imposes a constant strain ratio of $e_{xx} : e_{yy} : e_{xy} = 2 : 1 : 2$ corresponding to a proportional loading path. The second strain path corresponds to a non-proportional loading condition mentioned in Section 3.1.2. Stress components are plotted as functions of the applied strain in Figs. 20–24 for the proportional and non-proportional loading cases. Excellent agreement is observed between the *HCPD* model and homogenized micromechanical solutions for all cases.

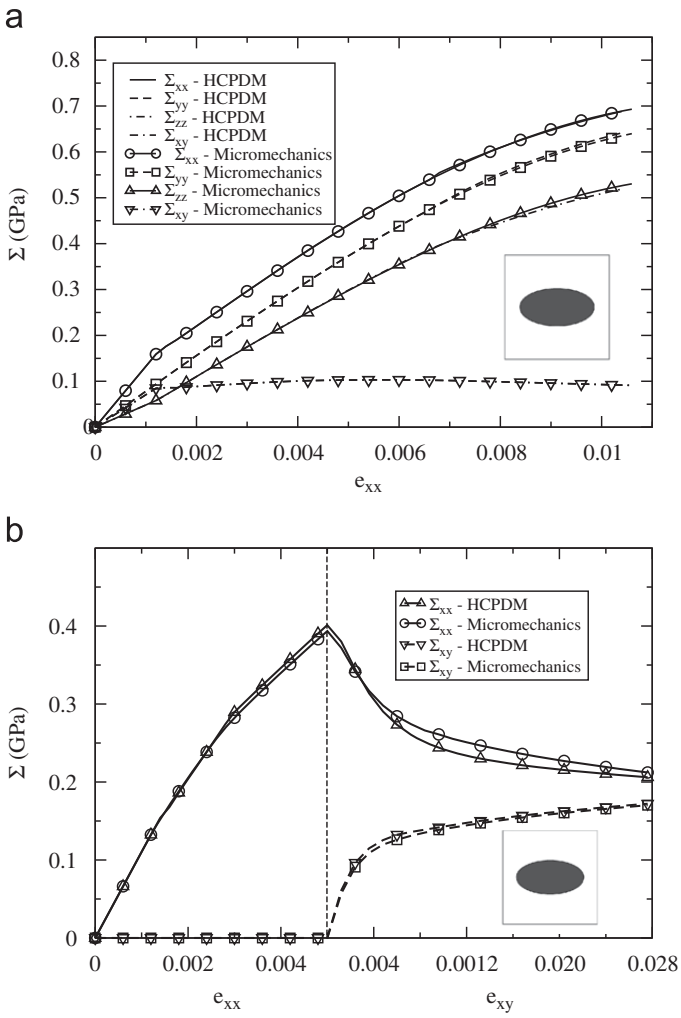

Fig. 21. Macroscopic stress–strain response by the HCPD model and homogenized micromechanical solutions for RVE (B): (a) $e_{xx} : e_{yy} : e_{xy} = 2 : 1 : 2$ and (b) non-proportional loading.

4.1.2. Validation of the void nucleation model

The void nucleation model is validated by simulating two different RVEs, shown in the insets of Fig. 25. Inclusions in one microstructure (A) have same size and are arranged in a cluster, while inclusions in microstructure (B) have a size probability density function of Eq. (28). Various parameters in the nucleation conditions of Eq. (25) are listed in Table 2. Because only plane strain problems are considered in this paper, the nucleation parameter C is not calibrated. Simulations are conducted for a number of different applied loads, both with the macroscopic HCPD model and micromechanical LE-VCFEM model. In simple tension, the stress in the transverse direction is zero. For both macroscopic and micromechanical analyses, the Von-Mises stress is plotted as a function of applied strains in Fig. 25. The micromechanical analyses show discrete drops in the stress level with the occurrence of each inclusion cracking. The macroscopic model, however, does not exhibit this discrete behavior due to continuous functions in the nucleation model. In general, results of the HCPD model analysis with nucleation follow the micromechanical analysis predictions quite closely, including the softening behavior due to loss of load carrying capacity. The figures show clearly that for both microstructural morphologies, the model predicts the nucleation induced behavior for loading in different directions quite accurately. The general agreement between the HCPD model and micromechanical analyses demonstrates the effectiveness of the nucleation relations in the constitutive model.

4.1.3. Macroscopic plate analysis

For the structural analysis, a square plate with a square hole under tension loading is analyzed both by the HCPD model and the microscopic LE-VCFEM model. A quarter of the plate with symmetry and load conditions is shown in Fig. 26(a). The microstructural RVE in Fig. 26(b) represents the unit cell RVE with 20% inclusion volume fraction. The dimensions of the plate and the unit cell are shown in the figures.

A total displacement of 4.5 μm is applied in 20 equal increments. The material properties are the same as in Section 4.1. Void nucleation is not considered in this simulation, and hence localization effects due to void nucleation do not occur. Only a local version of the HCPD model is used for macroscopic analysis. Fig. 26 shows the contour plots of void volume

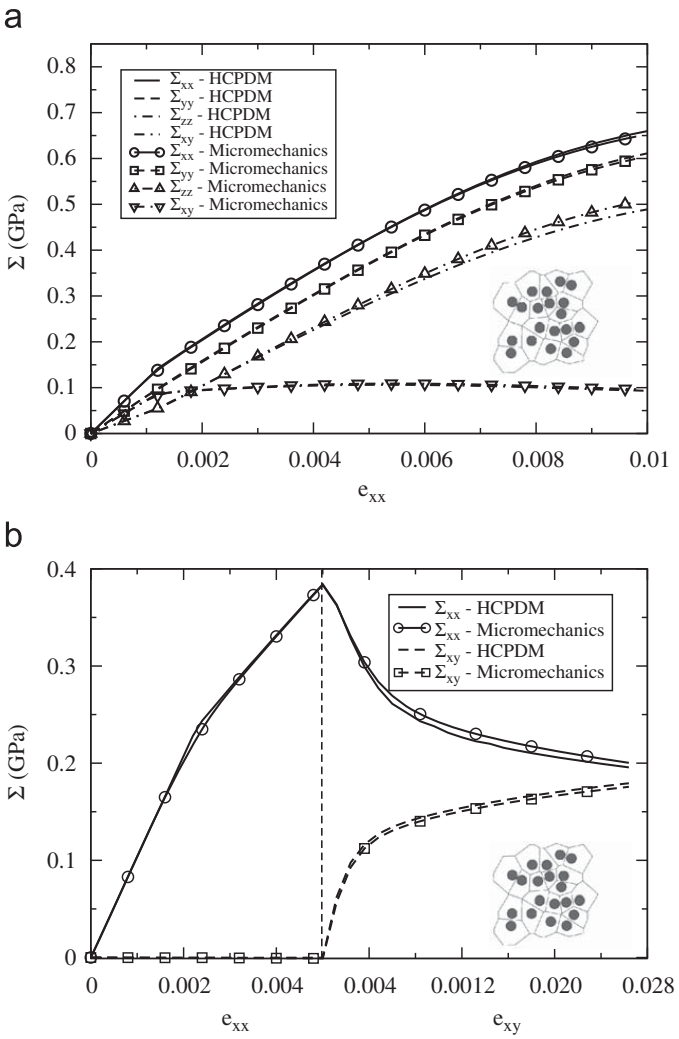

Fig. 22. Macroscopic stress–strain response by the HCPD model and homogenized micromechanical solutions for RVE (C): (a) $e_{xx} : e_{yy} : e_{xy} = 2 : 1 : 2$ and (b) non-proportional loading.

fraction obtained with the two models. These two figures show the same pattern of the distribution of void volume fraction. Additionally, the stress–strain history $\Sigma_{xx}-e_{xx}$ by the two models are compared at two locations in the plate (A, B), as shown in Fig. 27. While the agreement is excellent at location A, the difference between HCPD model and micromechanics is slightly more pronounced for location B due to the higher gradients of void volume fraction.

4.2. Simulation of a macroscopic plate with the non-local HCPD model

A rectangular plate, subjected to biaxial tension under plane strain conditions, is analyzed as shown in Fig. 29. Boundary conditions are prescribed as

$$\begin{aligned} &\text{at } x = 0: \quad u_x = 0, \quad \text{at } y = 0: \quad u_y = 0 \\ &\text{at } x = L_x: \quad u_x = U_x, \quad \text{at } y = L_y: \quad u_y = U_y \end{aligned} \tag{34}$$

where U_x and U_y are displacement components at the edges. The initial void volume fraction at the small square region of dimension w in the lower left corner is set to 0.01, while the rest of plate is initially void free. The material microstructure is represented by the RVE of Fig. 3(a), for which the HCPD model is developed. Material properties used are the same as in Section 4.1. To avoid mesh dependence of FEM solution, the non-local rate of void volume fraction expressed in Eq. (7) with the weighting function (8) is used in the HCPD model. The material characteristic length $L = 240\,\mu\text{m}$ is determined in Section 2.4. Near the boundary, the integral equation (8) involves material points outside of the computational domain boundary. Consequently, conditions of symmetry about the planes $x = 0$, $y = 0$, and periodicity about planes $x = L_x$ and $y = L_y$, as implied by Eqs. (34), are used to evaluate $\dot{f}_{local}$ from values inside the computational domain.

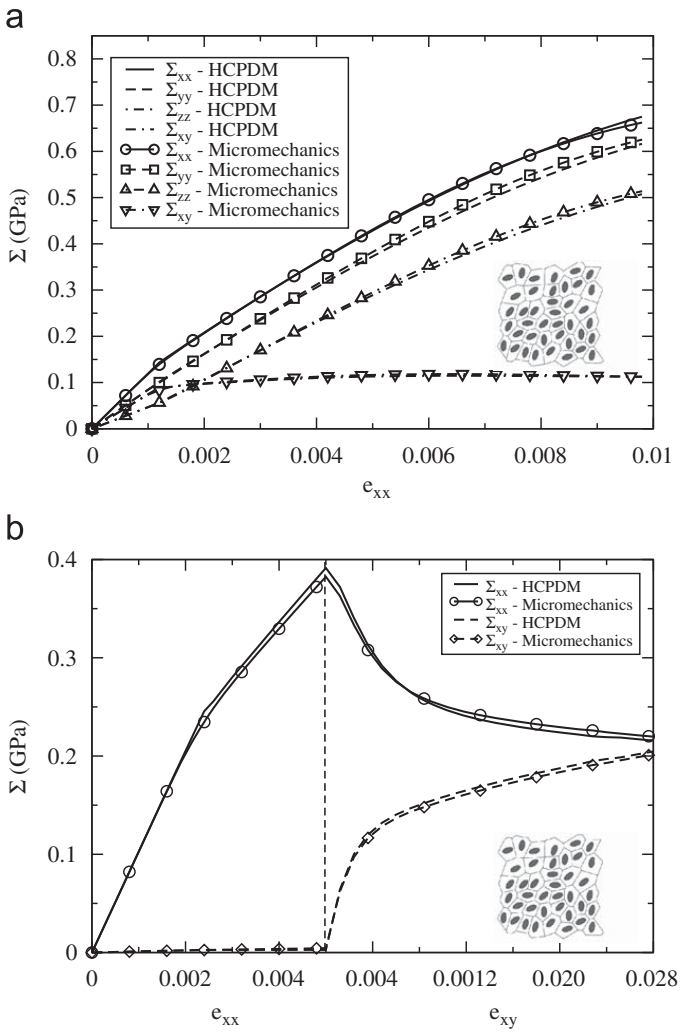

Fig. 23. Macroscopic stress–strain response by the HCPD model and homogenized micromechanical solutions for RVE (D): (a) $e_{xx} : e_{yy} : e_{xy} = 2 : 1 : 2$ and (b) non-proportional loading.

Also, updating the porosity f in each iteration step i requires evaluation of $\dot{f}_i$ in Eq. (7) from $\dot{f}_i^{local}$ in that step. Since values of $\dot{f}_i^{local}$ are not concurrently available at all the neighboring points, they are calculated from values in Eq. (7) at the end of the previous step as: $\dot{\bar{f}}_i = k_{i-1}\dot{f}_i^{local}$, where $k_{i-1} = \dot{\bar{f}}_{i-1}/\dot{f}_{i-1}^{local}$. In the event that $\dot{f}^{local}$ is very small ($\leqslant 10^{-8}$), k_{i-1} is taken to be unity. The loading step size should be small enough so that k_i at any integration point does not change substantially from step to step.

Results of simulations with the *HCPD* model with and without the non-local extensions are shown in Figs. 29 and 30 for a plate with dimensions $L_y = 2640\,\mu\text{m}$, $L_x/L_y = \frac{8}{11}$ and $w/L_y = \frac{1}{11}$. Two uniform meshes consisting of 16×22 and 32×44 elements, respectively, are considered for simulation with both the models. Prescribed displacement are $U_x = 345\,\mu\text{m}$ and $U_y = -160\,\mu\text{m}$. The equivalent stress–strain response of the lower-left corner element in the coarser mesh are compared in Fig. 28 for the local and non-local models. Onset of localization for the local model is much earlier than that in the non-local model. The contour plots of f in Figs. 29 and 30 show a considerable difference in behavior. For $L = 0$ in Fig. 29, a plastic localization band evolves due to void evolution. The bandwidth is clearly set by the mesh size and hence the results with the local model exhibit strong mesh dependence. On the other hand, mesh sensitivity is completely eliminated for the non-local model ($L = 240\,\mu\text{m}$) and results with both meshes in Fig. 30 show good agreement.

5. Conclusions

In this paper, an accurate and computationally efficient homogenization-based continuum plasticity-damage model is developed for macroscopic analysis of ductile failure in multi-phase porous ductile materials, such as cast aluminum alloys. The overall framework of the HCPD model follows the structure of an anisotropic Gurson–Tvergaard–Needleman elasto-porous-plasticity model for ductile materials. The model development uses a few important computational tools. These

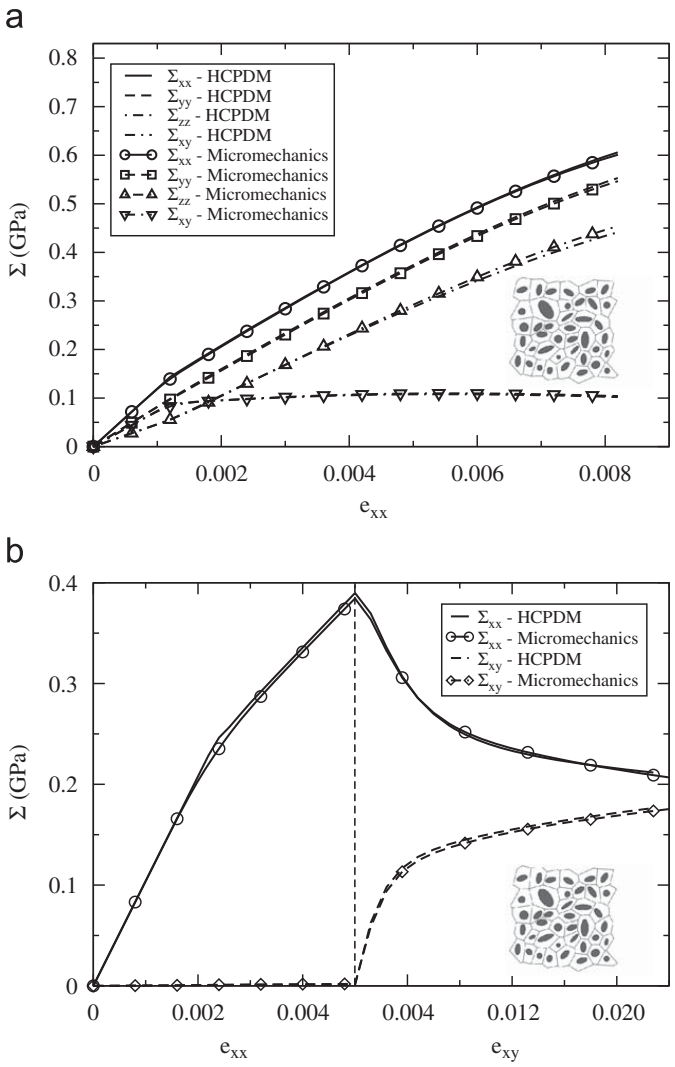

Fig. 24. Macroscopic stress–strain response by the HCPD model and homogenized micromechanical solutions for RVE (E): (a) $e_{xx} : e_{yy} : e_{xy} = 2 : 1 : 2$ and (b) non-proportional loading.

are: (a) LE-VCFEM-based micromechanical analysis model, (b) asymptotic homogenization methodology, (c) marked correlation for determining RVEs and (d) marked correlation function for determining non-local characteristic length. The *HCPD* model incorporates realistic estimates of RVE length scales in the microstructure, as well as non-local characteristic length scales in the macrostructure for removing mesh dependence. These length scales, obtained by statistical analysis and microstructural characterization, are necessary for modeling the ductile damage process at different scales.

Material anisotropy is determined not only by the morphology of the microstructure but also by the evolution of plastic deformation and damage. The orientation of the material principal coordinates can change significantly with the evolution of plastic deformation and damage. The effect is particularly pronounced for non-proportional load–strain histories. To account for this, the anisotropic HCPD model is expressed in the evolving material principal coordinate system and is assumed to remain orthotropic in it throughout the deformation history. The model parameters are calibrated from results of homogenization of microstructural variables obtained by LE-VCFEM analysis of the microstructural RVE containing inclusions, matrix and voids.

In contrast to conventional phenomenological models, the anisotropy parameters in the continuum model are found to evolve with plastic deformation in the microstructure. The dependence of these parameters on plastic work is nonlinear and diminishes with decreasing inclusion volume fraction. The functional forms of the parameters overcome serious limitations of constant anisotropy parameters that are conventionally assumed in anisotropic models. The model also incorporates a novel void nucleation criterion that is obtained by homogenizing micromechanical damage evolution by inclusion and matrix cracking. The uniqueness of the nucleation model is that it evolves from the distributions observed in the real microstructure, and has enough degrees of freedom to accommodate anisotropy with respect to inclusion cracking due to straining in different directions. Numerical examples are conducted for a variety of representative volume elements undergoing a wide range of proportional and non-proportional loadings. Comparison of the anisotropic HCPD model results with homogenized micromechanics results shows excellent agreement. Above all, the HCPD model has a huge efficiency

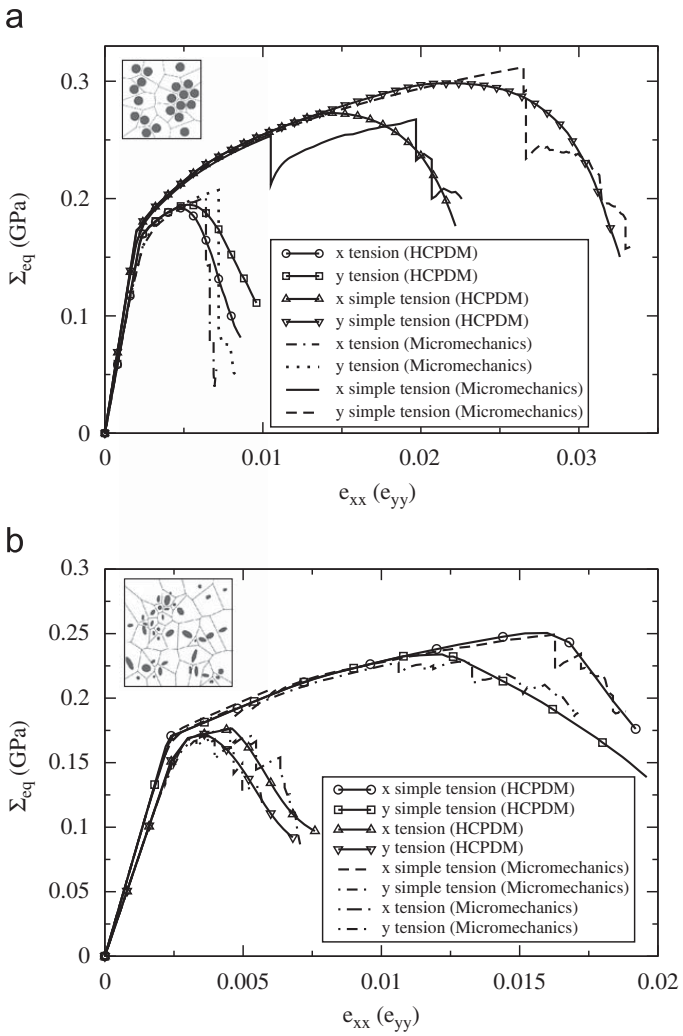

Fig. 25. Von-Mises stress–strain plot under different loading conditions with void nucleation model for (a) RVE (A) and (b) RVE (B).

Table 2
Void nucleation parameters in Eqs. (24) and (25) for two microstructures.

	e_0	m	A	B	C	D	E	F	V_p
RVE (A)	0.0082	9	1.05	1.06	–	−138.93	−136.28	68.88	4.50
RVE (B)	0.0090	3	1.86	1.78	–	−344.57	−370.87	179.52	0.20

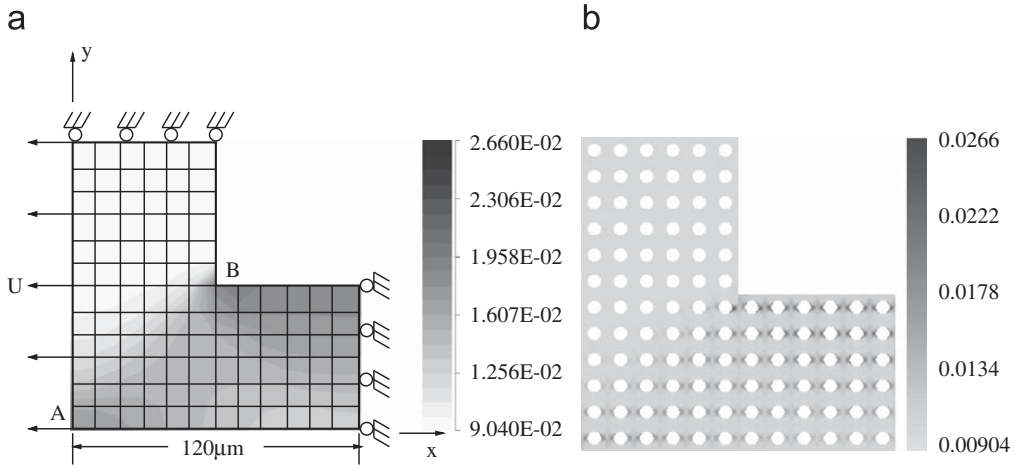

Fig. 26. (a) A square plate with square hole and contour plot of void volume fraction for HCPD simulations and (b) contour plot of void volume fraction for micromechanics simulation.

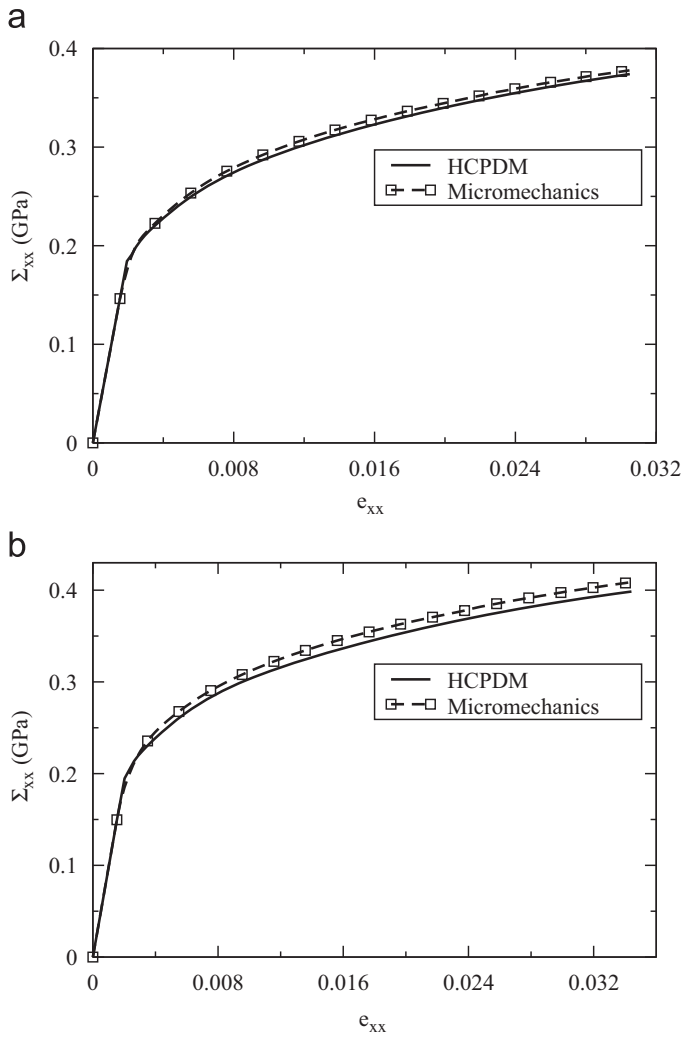

Fig. 27. Comparison of stress–strain behavior at two locations in the plate: (a) A and (b) B.

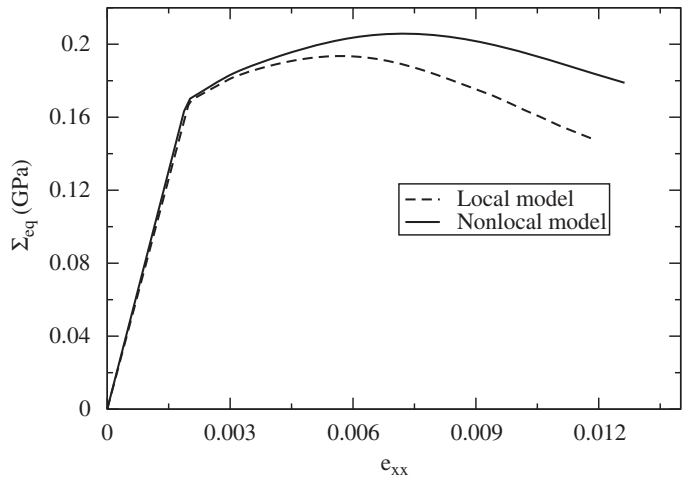

Fig. 28. Stress–strain response at the lower left corner element of the 16×22 element mesh, by the local and non-local models.

advantage over the micromechanics models and is hence a very effective tool in making macroscopic damage predictions in structures with explicit reference to the microstructural composition. This capability is largely lacking in the literature. The macroscopic behavior is sensitive to the shape, spatial arrangement as well as orientation of the inclusions. The model can be used in a material design framework to enhance the mechanical properties of structures/components by optimizing microstructural configurations and compositions.

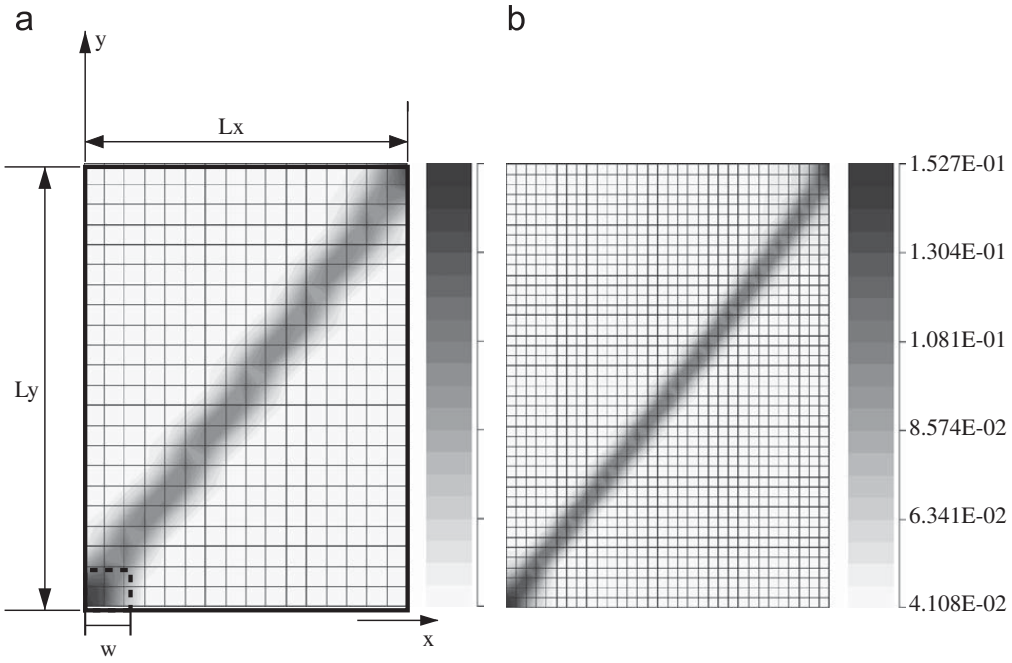

Fig. 29. Contour plots of void volume fraction for local model with two meshes: (a) 16 × 22 elements and (b) 32 × 44 elements.

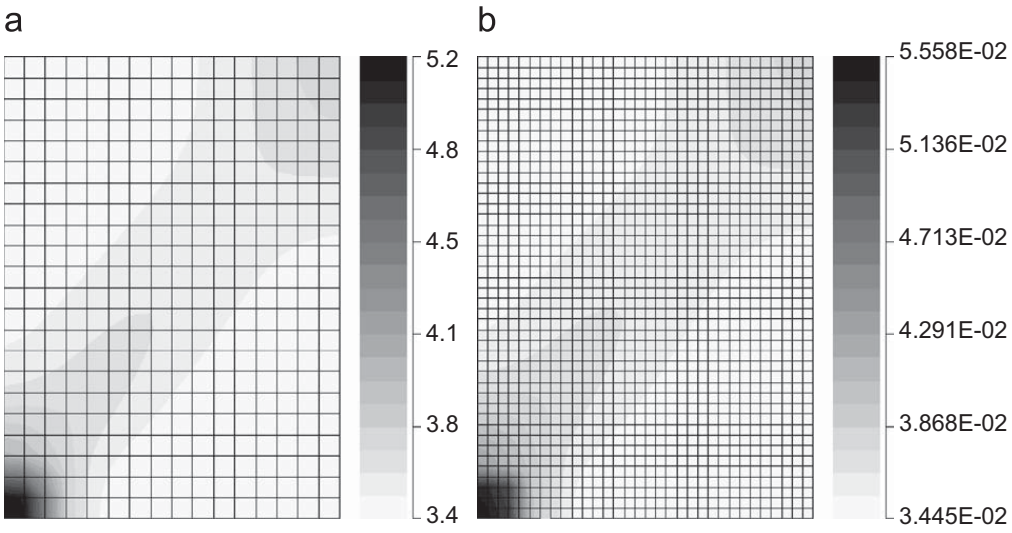

Fig. 30. Contour plots of void volume fraction for non-local model with two meshes: (a) 16 × 22 elements and (b) 32 × 44 elements.

Macroscopic analyses validate the success of the HCPD model. The need for such homogenization-based continuum models in multi-scale analysis for efficient, yet accurate analysis is inevitable. Yet, it is important to recognize the limitations of these models in representing highly localized damage evolution and cracks. This calls for localizing down the scales to capture local cracking at the microscale using top-down coupling. Such multi-scale framework for ductile fracture has been discussed in Ghosh et al. (2007) and Hu et al. (2007) for brittle failure and ductile failure in heterogeneous cast aluminum alloys.

Acknowledgments

This work has been supported by the National Science Foundation NSF Div Civil and Mechanical Systems Division through the GOALI Grant no. CMS-0308666 (Program director: C. Cooper) and by the Army Research Office through Grant no. DAAD19-02-1-0428 (Program Director: Dr. B. Lamattina). This sponsorship is gratefully acknowledged. Computer support by the Ohio Supercomputer Center through Grant PAS813-2 is also gratefully acknowledged.

References

Argon, A., Im, J., Sofoglu, R., 1975. Cavity formation from inclusions in ductile fracture. Metall. Trans. A 6A, 825–837.
Benssousan, A., Lions, J., Papanicoulau, G., 1978. Asymptotic Analysis for Periodic Structures. North-Holland, Amsterdam.
Benzerga, A., Besson, J., Pineau, A., 2004. Anisotropic ductile fracture Part II: theory. Acta Metall. 52, 4639–4650.
Caceres, C., 1999. Particle cracking and the tensile ductility of a model Al–Si–Mg composite system. Alum. Trans. 1, 1–13.
Chu, C., Needleman, A., 1980. Void nucleation effects in biaxially stretched sheets. J. Eng. Mater. Technol. 102, 249–256.
Devaux, J., Gologanu, M., Leblond, J., 1997. Recent extension of Gurson's model for porous ductile metals. Continuum Micromech. 377, 197–264.
Feyel, F., Chaboche, J., 2000. FE2 multiscale approach for modelling the elastoviscoplastic behaviour of long fiber SiC/Ti composite materials. Comput. Methods Appl. Mech. Eng. 183, 309–330.
Fish, J., Yu, Q., Shek, K., 1999. Computational damage mechanics for composite materials based on mathematical homogenization. Int. J. Numer. Methods Eng. 45, 1657–1679.
Garajeu, M., Suquet, P., 1997. Effective properties of porous ideally plastic or viscoplastic materials containing rigid particles. J. Mech. Phys. Solids 45, 873–902.
Ghosh, S., 2008. Multiscale Modeling and Simulation of Composite Materials and Structures. Springer, Berlin, pp. 83–164.
Ghosh, S., Bai, J., Raghavan, P., 2007. Concurrent multi-level model for damage evolution in microstructurally debonding composites. Mech. Mater. 39, 241–266.
Ghosh, S., Lee, K., Moorthy, S., 1995. Multiple scale analysis of heterogeneous elastic structures using homogenization theory and Voronoi cell finite element model. Int. J. Solids Struct. 32, 27–62.
Ghosh, S., Lee, K., Moorthy, S., 1996. Two scale analysis of heterogeneous elastic–plastic materials with asymptotic homogenization and Voronoi cell finite element model. Comput. Methods Appl. Mech. Eng. 132, 63–116.
Ghosh, S., Lee, K., Raghavan, P., 2001. A multi-level computational model for multi-scale damage analysis in composite and porous materials. Int. J. Solids Struct. 38, 2335–2385.
Ghosh, S., Moorthy, S., 1998. Particle cracking simulation in non-uniform microstructures of metal-matrix composites. Acta Metall. Mater. 46, 965–982.
Ghosh, S., Nowak, Z., Lee, K., 1997a. Quantitative characterization and modeling of composite microstructures by Voronoi cells. Acta Mater. 45, 2215–2234.
Ghosh, S., Nowak, Z., Lee, K., 1997b. Tesselation based computational methods for the characterization and analysis of heterogeneous microstructures. Comput. Sci. Technol. 57, 1187–1210.
Grange, M., Besson, J., Andrieu, E., 2000. An anisotropic Gurson type model to represent the ductile rupture of hydrided Zircaloy-4 sheets. Int. J. Fract. 105, 273–293.
Guedes, J.M., Kikuchi, N., 1990. Preprocessing and postprocessing for materials based on the homogenization method with adaptive finite element methods. Comput. Methods Appl. Mech. Eng. 83, 143–198.
Gurson, A., 1977. Continuum theory of ductile rupture by void nucleation and growth: Part I. Yield criteria and flow rule for porous ductile media. ASME J. Eng. Mater. Technol. 99, 2–15.
Hashin, Z., 1962. The elastic moduli of heterogeneous material. J. Appl. Mech. 29, 143–150.
Hill, R., 1948. A theory of yielding and plastic flow of anisotropic metals. Proc. R. Soc. London 193, 281–297.
Hu, C., Bai, J., Ghosh, S., 2007. Micromechanical and macroscopic models of ductile fracture in particle reinforced metallic materials. Modeling Simulation Mater. Sci. Eng. 15, 377–392.
Hu, C., Ghosh, S., 2008. Locally enhanced Voronoi cell finite element model (LE-VCFEM) for simulating evolving fracture in ductile microstructures containing inclusions. Int. J. Numer. Methods Eng. 76 (12), 1955–1992.
Jain, J.R., Ghosh, S., 2008a. A 3D continuum damage mechanics model from micromechanical analysis of fiber reinforced composites with interfacial damage. ASME J. Appl. Mech. 75 (3), 031011-1–031011-15.
Jain, J.R., Ghosh, S., 2008b. Damage evolution in composites with a homogenization based continuum damage mechanics model. Int. J. Damage Mech., doi:10.1177/1056789508091563.
Kouznetsova, V., Brekelmans, W., Baaijens, F., 2001. An approach to micro–macro modeling of hetergeneous materials. Comput. Mech. 27, 37–48.
Li, M., Ghosh, S., Richmond, O., 1999. An experimental–computational approach to the investigation of damage evolution in discontinuously reinforced aluminum matrix composite. Acta Mater. 47, 3515–3532.
Liao, K., Pan, J., Tang, S., 1997. Approximate yield criterion for anisotropic porous ductile sheet metals. Mech. Mater. 26, 213–226.
Llorca, J., Gonzalez, C., 1998. Microstructural factors controlling the strength and ductility of particle-reinforced metal-matrix composites. J. Mech. Phys. Solids 46, 1–28.
Moorthy, S., Ghosh, S., 1998. A Voronoi cell finite element model for particle cracking in elastic–plastic composite materials. Comput. Methods Appl. Mech. Eng. 151, 377–400.
Moorthy, S., Ghosh, S., 2000. Adaptivity and convergence in the Voronoi cell finite element model for analyzing heterogeneous materials. Comput. Methods Appl. Mech. Eng. 185, 37–74.
Mori, T., Tanaka, K., 1973. Average stress in the matrix and average elastic energy of materials with misfitting inclusions. Acta Metall. 21, 571–574.
Moulinec, H., Suquet, P., 1998. A numerical method for computing the overall response of nonlinear composites with complex microstructures. Comput. Methods Appl. Mech. Eng. 157, 69–94.
Moulinec, H., Suquet, P., 2001. A computational scheme for linear and nonlinear composites with arbitrary phase contrasts. Int. J. Numer. Methods Eng. 52, 139–160.
Pardoen, T., Hutchinson, J., 2000. An extended model for void growth and coalescence. J. Mech. Phys. Solids 48, 2467–2512.
Ponte Castaneda, P., Suquet, P., 1998. Nonlinear composites. Adv. Appl. Mech. 34, 171–302.
Pyrz, R., 1994. Quantitative description of the microstructure of composites: I. Morphology of unidirectional composite systems. Compos. Sci. Technol. 50, 197–208.
Raghavan, P., Ghosh, S., 2005. A continuum damage mechanics model for unidirectional composites undergoing interfacial debonding. Mech. Mater. 37, 955–979.
Sanchez-Palencia, E., 1980. Non-homogeneous Media and Vibration Theory, Lecture Notes in Physics. Springer, Berlin, Heidelberg.
Siruguet, K., Leblond, J., 2004. Effect of void locking by inclusion upon the plastic behaviour of porous ductile solids. Int. J. Plasticity 20, 225–268.
Terada, K., Kikuchi, N., 1995. Nonlinear Homogenization Method for Practical Applications, vol. 62. ASME, New York, pp. 1–16.
Terada, K., Kikuchi, N., 2001. A class of general algorithm for multi-scale analysis of heterogeneous media. Comput. Methods Appl. Mech. Eng. 190, 5427–5464.
Tvergaard, V., 1982. On localization in ductile materials containing voids. Int. J. Fract. 18, 237–251.
Tvergaard, V., Needleman, A., 1984. Analysis of cup-cone fracture in round tensile bar. Acta Metall. 32, 157–169.
Tvergaard, V., Needleman, A., 1995. Effects of nonlocal damage in porous plastic solids. Int. J. Solids Struct. 32, 1063–1077.
Vernerey, F., Liu, W., Moran, B., Olson, G., 2008. A micromorphic model for the multiple scale failure of heterogeneous materials. J. Mech. Phys. Solids 56, 1320–1347.
Wang, D., Pan, J., Liu, S., 2004. An anisotropic Gurson yield criterion for porous ductile sheet metals with planar anisotropy. Int. J. Damage Mech. 13, 7–33.
Wang, Q., 2003. Microstructural effects on the tensile and fracture behavior of aluminum casting alloys A356/357. Metall. Mater. Trans. A 34A, 2887–2899.
Willis, J., 1981. Variational and related methods for the overall properties of composites. Adv. Appl. Mech. 21, 1–78.